Title	Charge Stripe in FeTe
Author(s)	河島, 佑樹
Citation	北海道大学. 博士(工学) 甲第11874号
Issue Date	2015-03-25
DOI	10.14943/doctoral.k11874
Doc URL	http://hdl.handle.net/2115/68642
Type	theses (doctoral)
File Information	Yuki_Kawashima.pdf

Doctoral Thesis

Charge Stripe in FeTe

By Yuki Kawashima

Department of Applied Physics
Hokkaido University
Laboratory of Topological Science and Technology

Contents

Chapter 1

Introduction

1.1 Introduction

1.1.1 Charge stripe structure

How do we form a stripe structure using an isotropic interaction? An anisotropic interaction can create stripe patterns by ordering in the same direction. There are many anisotropic interactive elements such as electric dipoles in ferroelectric materials, directors in liquid crystals and magnetic dipoles. When the anisotropic interaction is composed of an attractive direction and a repulsive direction, the elements that have the anisotropic interaction form stripe structures [1, 2]. Can an isotropic interaction form a stripe pattern? Theoretically, isotropic particles can form a stripe pattern [3]. A coulomb interaction between charges is an isotropic interaction. However, it is said that the electron structure with the lowest energy is a triangle lattice called as Wigner crystal [4]. The rule of electrons in Wigner crystal is to keep distances between electrons far. This rule makes close-packed structure. How about electrons in a crystal? Experimentally, charge stripe structures have been discovered in several materials. One is organic conductors and another is Mott-insulator [5]. The charge stripe structure in organic materials is made by anisotropic lattice structure [6]. The charge stripe structure in Mott-insulators is made by rule of the minimizing antiferromagnetic domain wall by doping carriers [7]. The simple coulomb interaction is too simple to understand electronic structure in materials. In addition, electrons in these materials are like to localize. Then we do not have the stripe structure by metallic electrons which are far from localization. Is there charge stripe structure in metallic isotropic lattice crystal like Wigner crystal condition? However, this point is important, we do not have an answer in experiment. We should investigate and clarify the electronic structure made by Coulomb interaction in crystal.

Mechanism of charge stripe in organic conductors

In this section, I introduce why the charge stripe is occurred in organic conductors [6]. There are many types of the ground state appear in the organic conductors. This is because the kinds and arrangements of molecule have some varieties. The charge order is one of the ground state in organic conductors [5]. The charge stripe structure one of the charge order is occurred in two dimensional organic conductors. Now we make sure of character of electrons in organic conductors. The carrier density on organic conductors like (BEDT-TTF)$_2$I$_3$ is fixed by proportion between cationic organic molecular and anionic materials. Usually, the proportion between them is 2:1. Then electronic band filling is quarter filling in organic conductors without dimerization. In addition, organic conductors is strong correlated material. Because low carrier density is made by the large molecular and weaken the screening of Coulomb interaction. The long range coulomb interaction makes charge order in organic conductors. However, the structure strong depends on the molecule arrangement. Typical charge ordering material is α type (BEDT-TTF)$_2$I$_3$. Anisotropic molecular arrangement makes one dimensional electronic arrangement as charge stripe.

Mechanism of charge stripe in Mott-insulator materials

In this section, I introduce why the charge stripe is occurred in Mott-insulator materials. Localized electrons in Mott-insulators are caused by the strong on-site Coulomb interaction. Band filling of Mott-insulator is half filling. Electrons in Mott-insulators localize on each site and make antiferromagnetic structure. The charge stripe structure had been predicted theoretically [7] as the pattern formed by carriers in Mott-insulators. Cuprate superconductors which are famous Mott-insulator materials have a charge stripe structure [8, 9]. The stripe structure on cuprate superconductors was found as doped carrier with insulating antiferromagnetic domains [8]. Similarly to cuprate superconductors, the charge stripe was found in other transition metal oxides such as nickelates [10], manganites [11, 12] and cobaltates [13]. In these materials, holes form a stripe structure to minimize the antiferromagnetic domain wall. It is important that the stripe structure in Mott-insulator is stabilized only at commensurate period [14, 15, 16, 17]. The main character of charge stripe structure on Mott-insulator is fixed by Mott insulator background.

To study the isotropic interactive metallic stripe structure connecting with Wigner crystal, we need more simple electronic system.

1.1.2 Iron-based superconductors

The history of the superconductivity starts at measurement of resistivity at very low temperature on mercury using liquid helium by H. K. Onnes in 1911. Many kinds of superconductor have been discovered such as simple elements, alloys, heavy fermions, organic conductors, fullerenes and cuprate oxides. New type superconductors, which have different superconducting mechanism from Bardeen-Cooper-Schrieffer (BCS) theory, belong with strong correlated system. It is said that strong magnetic elements like transition metals could not show the superconductivity, because magnetic impurity strongly destroy the superconductivity. But superconductors LaFePO and $\mathrm{LaFeAsO}_{1-x}\mathrm{F}_x$ on which conductive electrons are on iron element were discovered on 2006 by Y. Kamihara and H. Hosono [18, 19]. These materials were named iron-based superconductors. Iron-based superconductors have different type of crystal structures including RFePnO (R = Rare Earth metals, Pn = P, As) [18, 19], (Ba, K)$\mathrm{Fe}_2\mathrm{As}_2$ [20], LiFeAs [21] and $\mathrm{FeSe}_{1-\delta}$ [22]. The superconducting transition temperature of the iron-based superconductor is higher than 40 K for $\mathrm{RFeAsO}_{1-x}\mathrm{F}_x$ [23, 24, 25]. Therefore, the iron-based superconductor is called a new high T_c superconductor. The phase diagram was studied in a wide range of doping level by hydrogen substitution on LaFeAsO [26]. The iron-based superconductor has two-dimensional a crystal structure and Fermi surfaces [27, 28]. It is said that the hole Fermi surface at the Γ point and the electron Fermi surface at the M point induce a spin density wave (SDW) transition as a result of Fermi surface nesting [29, 33]. It is noteworthy that direct evidences of SDW such as collective excitations have not been observed yet. Figure 1.1 and 1.2 shows the phase diagram of $\mathrm{LaFeAsO}_{1-x}\mathrm{F}_x$ and $\mathrm{Ba}_{1-x}\mathrm{K}_x\mathrm{Fe}_2\mathrm{As}_2$, respectively. Even if there are difference on the method of controlling the phase between $\mathrm{LaFeAsO}_{1-x}\mathrm{F}_x$

and $Ba_{1-x}K_xFe_2As_2$, the main behavior of the phase diagrams are the same. The phase diagram of the iron-based superconductors reveal the coexistence of the antiferromagnetism and superconductivity [19, 34, 35, 36]. It is important that superconductivity is very close to the magnetism in iron-based superconductors [37]. One can imagine that the superconductivity has a magnetic origin in iron-based superconductors. Itinerant antiferromagnetic ordered phases are stable for mother compound of iron-based superconductor [37, 38], unlike high T_c cuprates, of which magnetic phase is the Mott insulator. Studying the magnetic phase can clarify the origin of the superconductivity in iron-based superconductors. Figure 1.3 shows the phase diagram of the cuprate superconductors. At the point of existence of magnetism and superconductivity, iron-based superconductors are similar to organic conductors and cuprate superconductors. An organic conductor and a cuprate superconductor forms a charge order which usually competes with superconductivity. Then iron-based superconductors may form a charge ordering structure competing with superconductivity.

I propose the phase diagram for iron-based superconductors as a function of the spin-spin interaction as shown in Fig. 1.4. Spins in magnets are ordered by strong inter-spin interaction. The ground state in magnets is brought about by spins. Suppressing the inter-spin interaction, which is brought by large spin moment in magnetic elements, might make the system superconducting even though the system consists of magnetic elements. In the case of a weak inter-spin interaction, the charge degree of freedom brings about the attractive force which causes the superconductivity. Therefore, charges bear the ground state in the superconducting phase in iron-based superconductors. The ground state, where both the charge and spin degree of freedoms play important roles, is thought to exist between the magnetic and superconducting phase in iron-based superconductors. I focus on such an intermediate phase between the magnetic and superconducting phase. There is no intermediate phase in cuprate and organic superconductors. The intermediate phase in iron-based superconductors is supposed to contain new electronic states. The spin density wave (SDW) is the ground state which has both charge and spin degree of freedom. It is suggested that SDW occurs in non-superconducting phase in iron-based superconductors [29]. I suppose that the SDW relates strongly with the electronic in the intermediate phase.

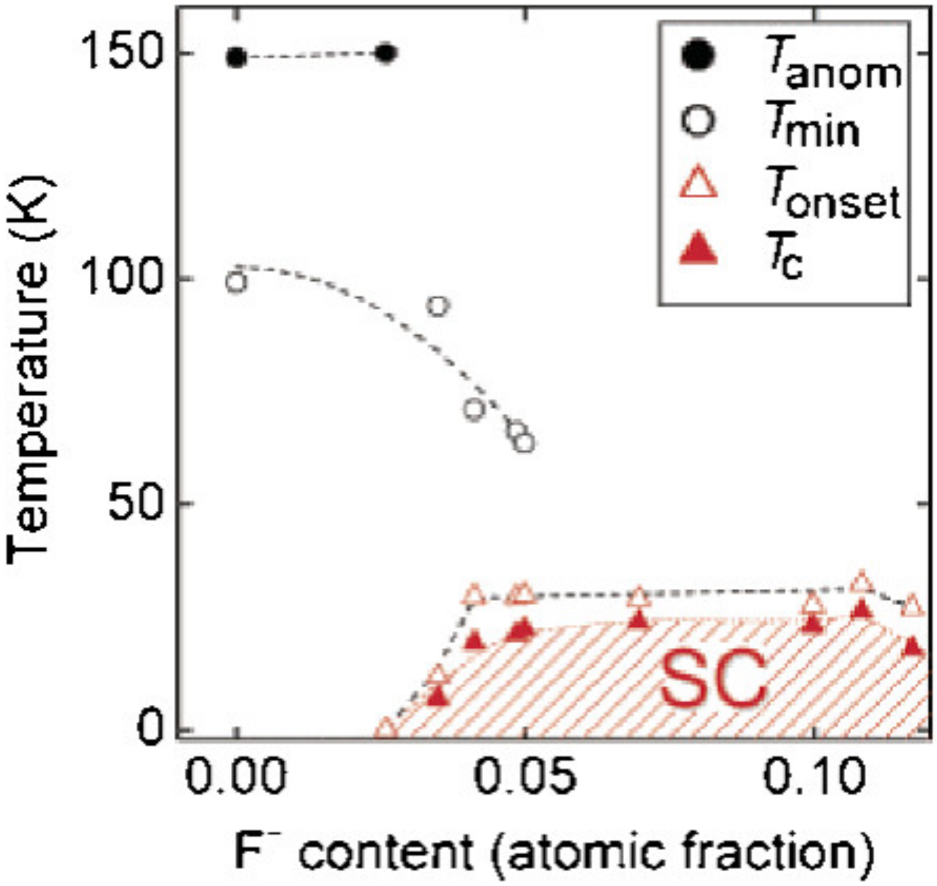

Figure 1.1: The phase diagram of $LaFeAsO_{1-x}F_x$ [19].

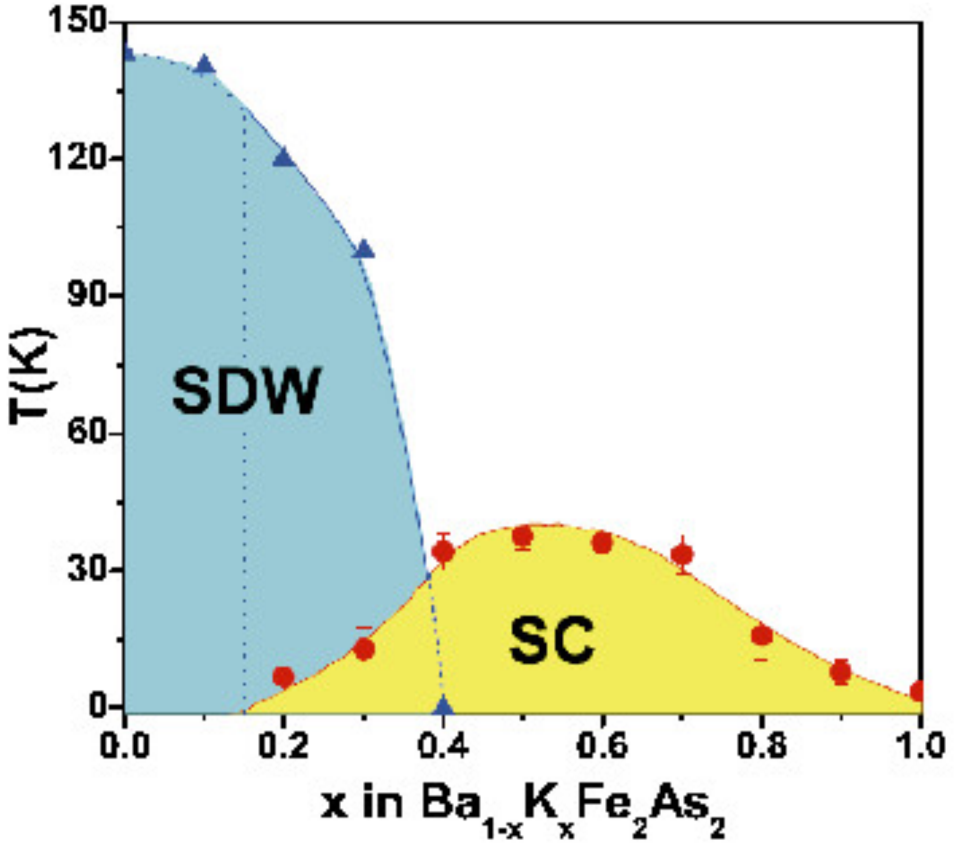

Figure 1.2: The phase diagram of $Ba_{1-x}K_xFe_2As_2$ [34].

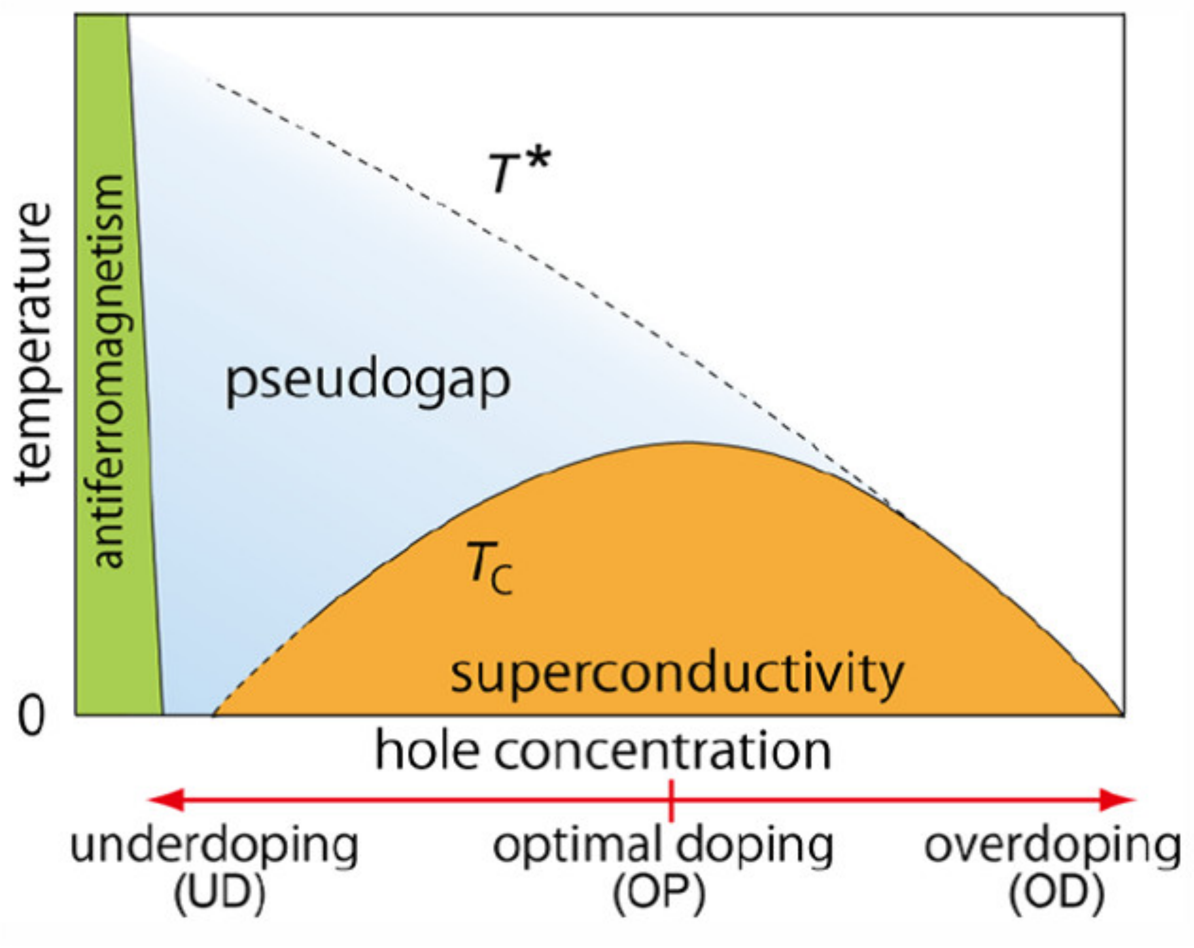

Figure 1.3: The phase diagram of the cuprate superconductor.

1.1.3 Density waves

The density wave state is one of the electronic ground states in low dimensional materials. There are two types of density wave corresponding two degree of freedom on electron. One is charge density wave (CDW). Another is spin density wave (SDW).

Response fuction and Fermi surface nesting

Density waves are explained by response function. Free electron Hamiltonian is written as

$$H_0 = \frac{\hbar^2 k^2}{2m} \tag{1.1}$$

Response function appears by adding wave form potential energy

$$V = V_Q \mathrm{exp(iQr)} \tag{1.2}$$

The density modulation ρ_Q and response function $\chi_(Q)$ is written by the amplitude of potential energy V_Q

$$\rho_Q = -\chi(Q) \times V_Q \tag{1.3}$$

$$\chi(Q) = \sum_k \frac{f_{k+Q} - f_k}{E_k - E_{k+Q}} \tag{1.4}$$

f_k: Fermi distribution function

At T=0, $f_{K+Q} - f_K$ have a value only f_{k+Q}=1 and f_k=0 or f_{k+Q}=0 and f_k=1. This means electron can be excited by the potential energy with wave number Q. In this case, the response function depends on how many electrons can be excited by the potential with only wave number Q. Response function is easily considered by the Fermi surface. If a Fermi surface moves Q and overlaps other Fermi surface, the response function becomes large. The overlap of Fermi surface is called nesting. Figure 1.5 shows one dimensional Fermi surface. Figure 1.5 shows the overlap of Fermi surface is large on one dimensional Fermi surface. Then electrons on one dimensional Fermi surface response to potential energy and make density wave with wave number Q. Density wave occurs in large response function corresponding to large overlap of Fermi surface called nesting. The electrons are effected by new period potential with Q and energy gap opens at Fermi energy.

Spin Density Wave

Different interaction make different type of density wave in material. Electron-phonon interaction and on-site Coulomb interaction make CDW and SDW, respectively. In strong correlated materials, the on-site Coulomb interaction is strong. Then SDW appear at strong correlated materials. Figure 1.6 shows schematic diagram of SDW. The spin density modulates in space. There are two differences between CDW and SDW. One is that, because the spin has degree of freedom of spin up and spin down, local moment which correspond to local spin density can take positive and negative. Another is that the order parameter and excitation of SDW has degree of freedom of spin texture. A typical SDW material is organic conductors such as $(\mathrm{TMTSF})_2\mathrm{X}$ (X=$\mathrm{AsF_6}$,$\mathrm{PF_6}$) [30, 31, 32]. Iron-based superconductor is strong correlated material and said having Fermi surface nesting. Then it is said that iron-based superconductor have SDW phase [27, 28, 29, 33].

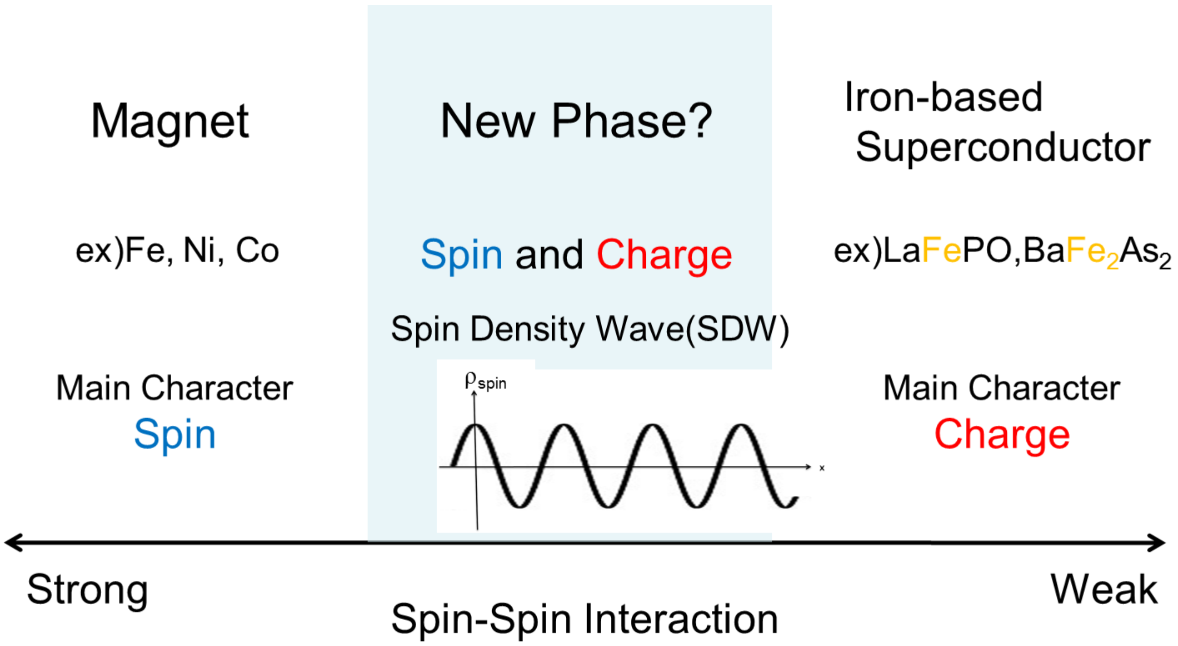

Figure 1.4: The schematic diagram of Iron-based superconductor from spin-spin interaction.

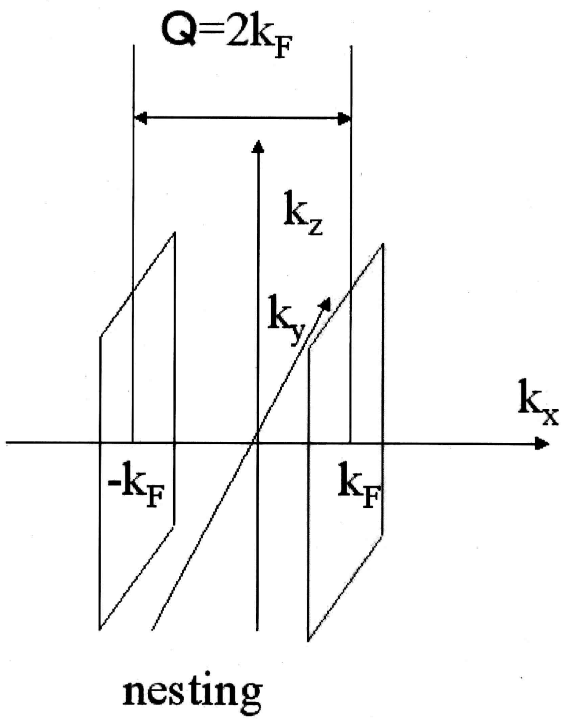

Figure 1.5: One dimensional Fermi surface

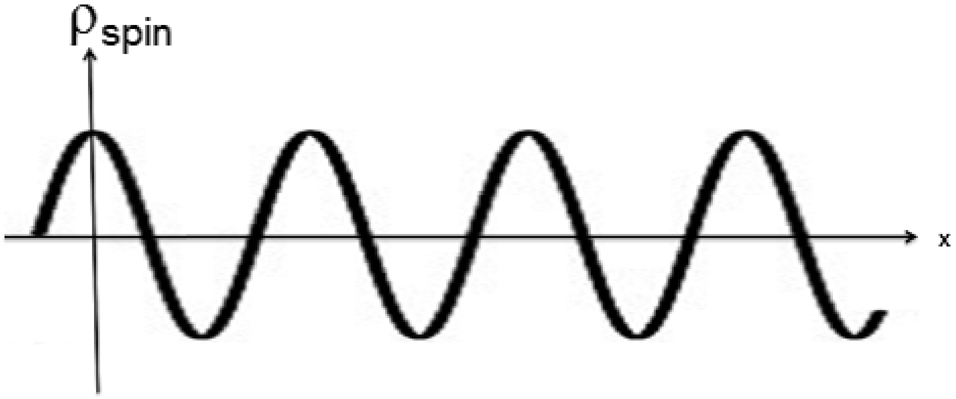

Figure 1.6: The schematic diagram of SDW.

1.1.4 FeX (X=S,Se,Te)

Iron-based superconductors are distinguished by kind of insulating and conductive layer. For example, LaFePO, first material of iron-based superconductor, has conductive layer on Fe and P and insulating layer on La and O. FeX series have simplest structure among iron-based superconductors. In FeX, Te conductive layer on Fe and X and no insulating layer. Figure 1.7 shows phase diagram of $FeTe_{1-x}Se_x$. FeTe does not show the superconductivity without substituting Te with Se. The superconducting transition temperature appears and rises up to 13 K by substituting Te with Se. The main structure of phase diagram of Fig. 1.7 is the same as Fig. 1.1 and 1.2. Then FeTe corresponds to mother material in iron-based superconductor, however there are difference between what element connect to Fe. Since FeX has no blocking layer, it is suitable to study the electronic state of the conducting layer. Figure 1.7 shows phase diagram of $Fe_{1+x}Te$. The carrier concentration is controlled by excess iron. There are three phase in FeTe distinguished by crystal structure and magnetic structure. FeTe is best material to study non-superconducting phase among iron-based superconductors.

1.2 Purpose of this study

Experimental purpose of this study is revealing the charge structure of iron-based superconductor and discussing as new type of electron correlating material.

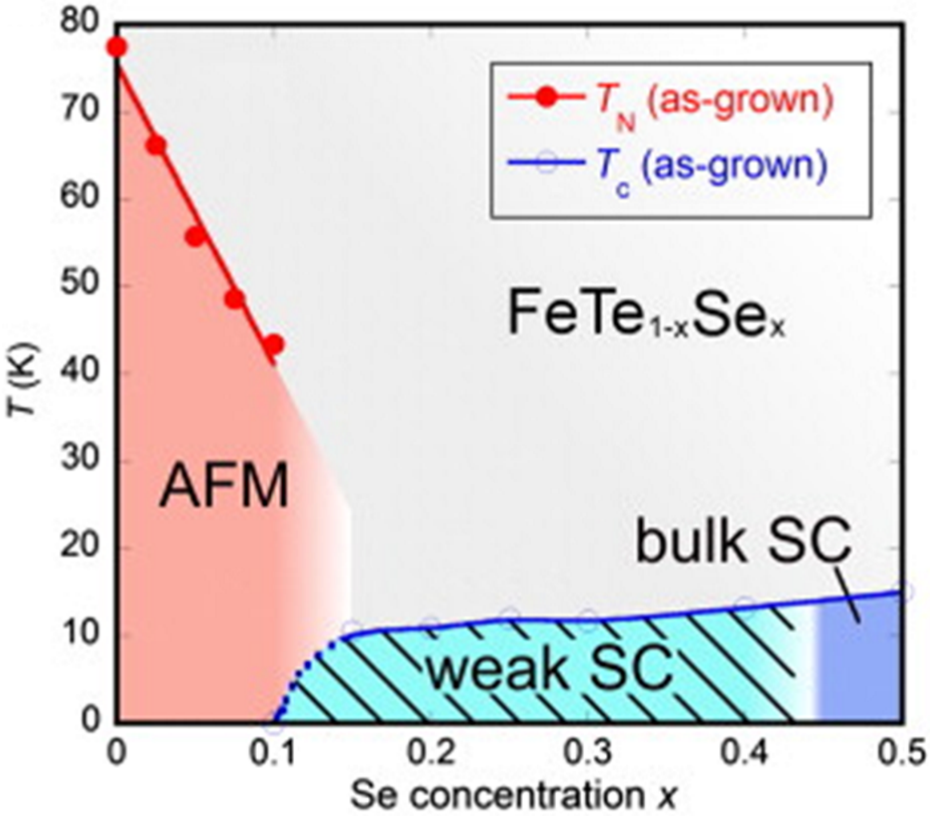

Figure 1.7: The phase diagram of $FeSe_xTe_{1-x}$ [39].

Chapter 2

Experimental methods

2.1 Sample preparation

Single crystals of $Fe_{1+x}Te$ were grown by chemical vapor transport method with using iodine.

Raw materials

Fe: Kojundo chemical laboratory co. purity 99.5%up wire
Te: Nilaco purity 99.9999% small chunk
I: Wako Pure Chemical Industries, Ltd. purity 99.9% small chunk

Synthesis and crystal growing

The ampule was made from straight quartz silica tube with 8 mm inner diameter. The quartz tube and the iron was evacuated about 10^{-4} Pa and baked for purify. After purify, the silica tube was sealed as shown in Fig. 2.1. Sum of the iron and tellurium was put about 1 g and iodine transport agent was put a few milligrams. It should be take care about the iodine subliming. It causes pollution of the evacuation system. The ample suld be made as soon as possible after putting an iodine.

Single crystals were grown at 600∼700 °C for a week by electronic furnaces. $Fe_{1+x}Te$ single crystals with 1 square mm were obtained. Fig. 2.2 shows typical obtained sample. The single crystalline sample in fig. 2.2 has corners corresponding with crystal axis. I get good crystalline sample by my synthesis method. Fig. 2.3 shows cleaved surface for STM experiment taken by FE-SEM. The surface inside of the red lines indicates cleaved a sample surface. I cannot detect asperity on the sample by FE-SEM measurement. The sample shows flat surface from FE-SEM measurement. Then $Fe_{1+x}Te$ is very good sample for using STM. The composition of obtained sample was characterized roughly by EDS. The amount of an excess iron x was determined by ICP-AES with accuracy of two places of decimals. A excess iron increases by increasing synthesis temperature. Crystal structure was determined by X-ray diffraction.

Figure 2.1: Schematic view of ample used for the chemical vapor transport with using iodine as the transport agent.

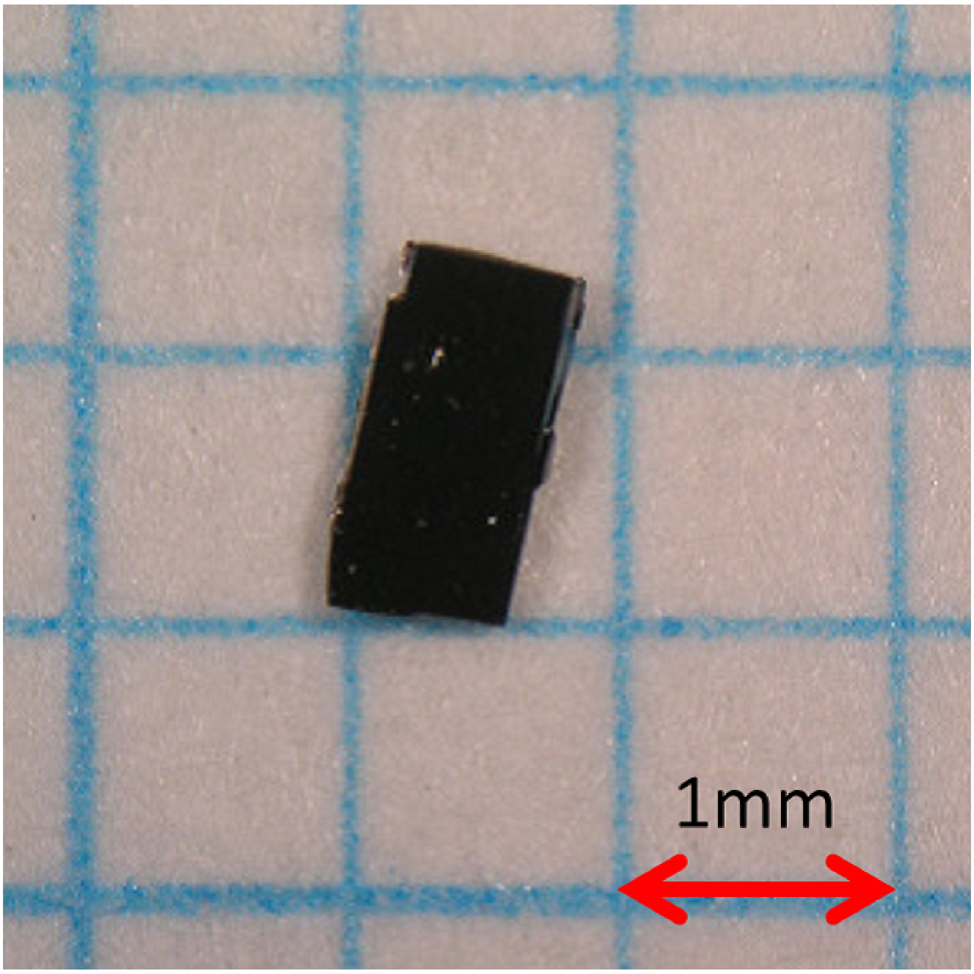

Figure 2.2: Typical single crystal picture of $Fe_{1+x}Te$ obtained by the chemical vapor transport.

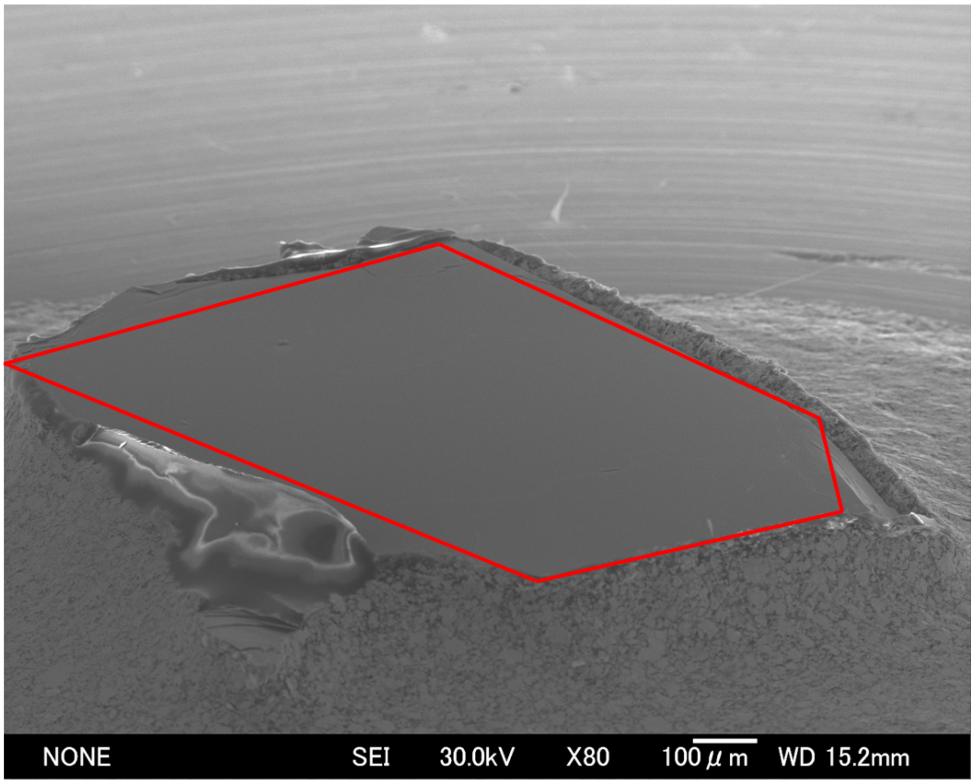

Figure 2.3: FE-SEM picture of cleaved $Fe_{1+x}Te$ surface. The surface inside of the red lines indicates cleaved a sample surface. This picture is taken from slanted angle.

2.2 Sample characterization

2.2.1 Composition analysis

The composition was determined by energy dispersive x-ray spectroscopy (EDS) and inductively coupled plasma atomic emission spectroscopy (ICP-AES). However EDS can measure the composition ratio in sample, the accuracy is not enough to determine less quantity of doping. Then ICP-AES is needed to decide less quantity of doping.

2.2.2 Magnetic susceptibility measurement

Static magnetic susceptibility was measured by SQUID magnetometer. The sample was fixed on non-magnetic polymer thin wire using STYCAST1266.

Apparatus
Manufactured by QuantumDesign, Model MPMSXL
Temperature range 2∼300 K
Magnetic field range -7∼7 T

2.2.3 Resistivity measurement

Temperature dependence of the resistivity was measured on grass He vessel by DC 4 probe method.

Apparatus
DC voltage/current source: Manufactured by YOKOGAWA, Model 7651 Programmable DC Source
Digital multimeter: Manufactured by KEITHLEY, Model 182 Sensitive Digital Voltmeter

2.3 Scanning tunneling microscopy/spectroscopy (STM/STS)

2.3.1 Principle of the STM/STS

With use of an STM, we can obtain the energy spectra of the density of states with high energy resolution by measuring tunneling differential conductance, and the electron density with the spatial resolution of nano scale. Figure 2.4 shows a schematic view of STM. The tunneling current depends on the distance and applied bias voltage between tip and sample. Either keeping tunneling current and measuring distance or keeping distance and measuring tunneling current on scanning sample surface make atomic resolution sample surface picture.

STM

The tunneling current between tip and sample is given by WKB approximation as

$$I = \frac{abV\phi^{1/2}}{d} exp(-ad\phi^{1/2}) \tag{2.1}$$

$$a = \frac{4\pi(2m)^{(1/2)}}{h} = 10.25(nm)^{(-1)}(eV)^{(-1/2)}$$

$$b = \frac{e^2}{4\pi h}$$

m: mass of electron e: coulomb of electron
V: bias voltage
ϕ: work function

While the length between tip and sample change 1 nm, the tunneling current change a order. Then we can get atomic resolution on sample surface by scanning.

STS

In the case of the tunneling junction between two different material. The tunneling current I from sample A to sample B on bias voltage V shows as

$$I = \frac{4\pi e}{\hbar}\int_{\infty}^{-\infty} |M|^2 D_A(E) D_B(E+eV)[f(E) - f(E+eV)]dE \tag{2.2}$$

M: tunneling matrix element

$D_A(E), D_B(E)$: the density of state for samples A, B

$f(E)$: Fermi distribution function

This equation consists on tunneling junction experiments (ex. break junction method). If we use normal metallic tip as sample B, $D_B(E)$ is constant near the Fermi energy. Additionally, |M| is constant on this range. The tunneling differential conductance is given

$$\frac{dI}{dV} = \frac{4\pi e^2}{\hbar}|M|^2 D_B(0)\int_{\infty}^{-\infty} D_A(E)[-\frac{\partial f(E+eV)}{\partial V}]dE \tag{2.3}$$

The Fermi distribution function can be approximated as delta function at low temperature. Then we get

$$\frac{dI}{dV} \propto D_A(-eV) \tag{2.4}$$

The tunneling differential conductance is proportional to the sample A. We can get the energy dependence of the density of state on sample by varying the bias voltage. The feature of STS experiment is tunneling barrier. Vacuum makes tunneling barrier on STS whenever measure any sample.

2.3.2 Experimental apparatus and preparation on STM

I used temperature variable ultra high vacuum (UHV)-STM. Samples can be cleaved at ultra high vacuumed chamber. Figure 2.5 shows crystal structure view from parallel to *a*-*b* plane in FeTe. The sample is cleaved parallel to *a*-*b* plane in FeTe. Then we can get flesh and flat surface on FeTe. This point is important on STM to measure atomic resolution. The sample was fixed on and took conductivity to copper plate sample holder by silver epoxy adhesive agent (EPO-TEK. Model E4110). That solidification takes two hours at 200 Celsius degree. A non-magnetic cleaving rod with 1mm diameter was prepared and was fixed on the sample with Araldite. Cleaved sample surface was kept clean from absorption of and reaction with the air molecule in this cleaved environment.

Apparatus

Base unit: Insert type ultra low temperature STM unit (Unisoku Co.), Model USS-7920LTU

Controller: SPM controller basic unit (RHK Co.), Model USM100RH

Tip: Pt: Ir tip (Unisoku Co.)

Vacuum: 10^{-8}Pa

Achieving temperature: 7.0 K

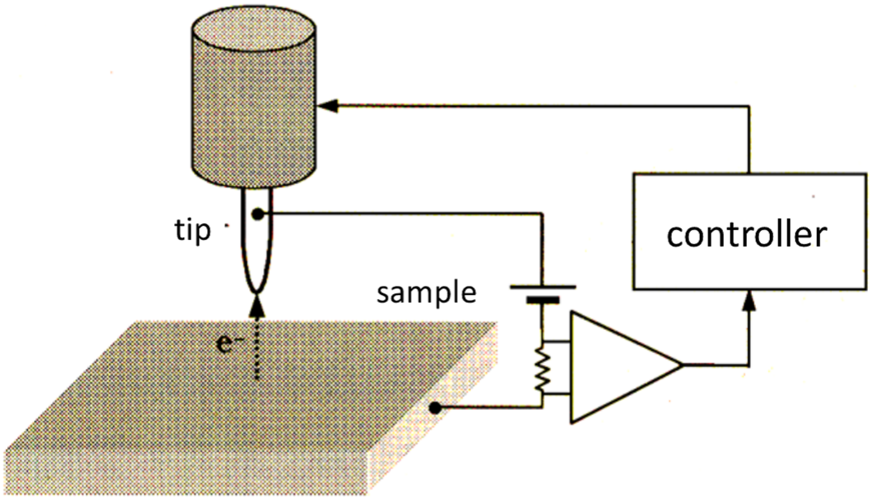

Figure 2.4: Schematic picture of STM. In this case, the tip is fix at piezo actuator and bias voltage apply to the tip.

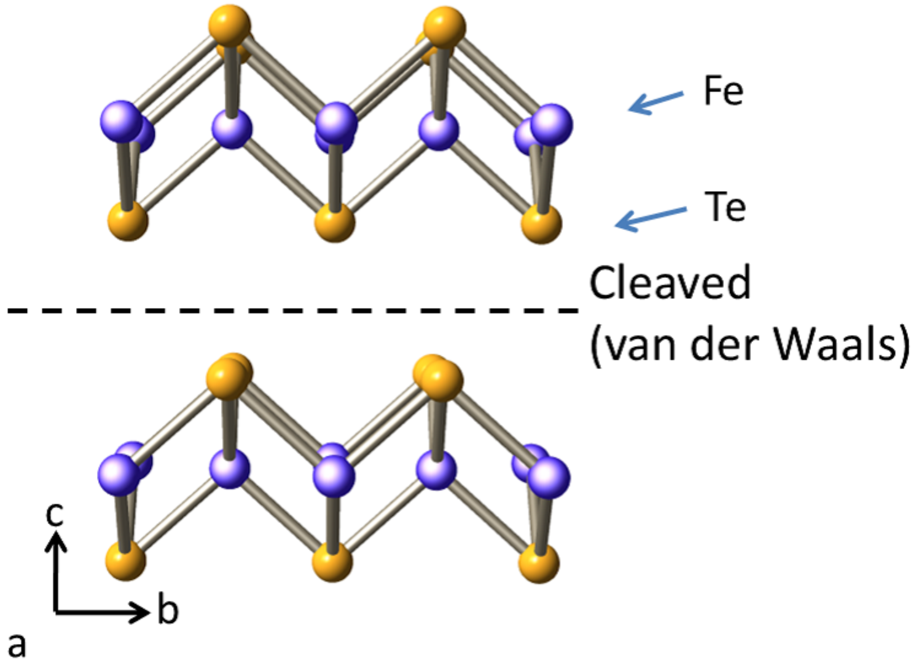

Figure 2.5: Crystal structure of FeTe. Dash line shows cleavage plane.

2.4 Femtosecond time-resolved reflection measurements

By femtosecond time-resolved reflection measurements, we can get reflectivity of excited electron state with time resolution of femtosecond resolution. The resolution is controlled by width of the light pulse. Usually the resolution is a few dozen fs. On the other hands, the time scale of electron relaxation over 1 ps. Then we can get the relaxation dynamics of the excited electrons by using femtosecond time-resolved reflection measurements. The transient reflectivity is given as a function of times as follows:

$$\Delta R(t,T) = A(T)e^{t/\tau_A} + B(T)e^{t/\tau_B}cos(\omega_B t) + C(T) \tag{2.5}$$

where first term corresponds to the single-particle decay via the band gap. Magnitude of transient reflectivity A(T) corresponds to the number of electrons excited by pump pulse. Transient time τ_A shows a lifetime of excited electrons. If there is a gap structure on the Fermi level, excited electrons give energy to optical phonons and go back to the initial state (Fig. 2.7 Process 1). Optical phonons give energy in two ways. One is giving energy to electrons in valence band (Fig. 2.7 Process 2). Another is giving energy to acoustic phonons (Fig. 2.7 Process 3). The probability of electron excitation by optical phonons has inverse relation to the gap size. When the gap size is large, the probability of electron excitation by optical phonons reduces. This appears as short transient time. Second term corresponds to coupling with excited coherent phonons. The oscillation frequency corresponds to the phonon mode. Coherent phonons reduce energy by giving other phonons. Then the oscillation decays with characteristic transient time. Coherent phonons appear in some materials. For example, fig 2.6 shows coherent phonon mode on GaAs (100) surface [40].

2.4.1 Two color pump probe measurement

Figure 2.8 shows a schematic illustration of the femtosecond time-resolved reflection measurement system. The light pulse source in this system is mode-lock Ti:sapphire laser. The laser from source ($\lambda = 800$ nm) splits into pump pulse and probe pulse by the beam splitter. The wavelength of the pump pulse change to 400 nm at LBO (LiB_3O_5) crystal. When the wavelength of the pump pulse is different to that of probe pulse, these pulses

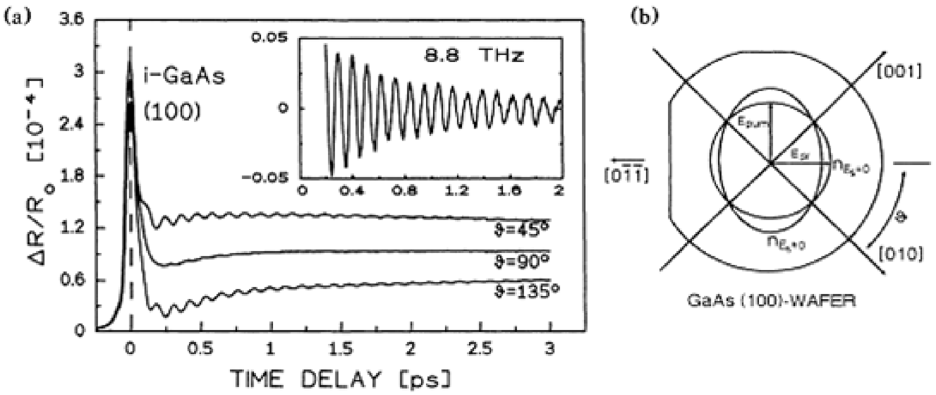

Figure 2.6: Coherent phonon mode on GaAs (100) surface. Reflectivity oscillation correspond to excited coherent optical phonon mode [40].

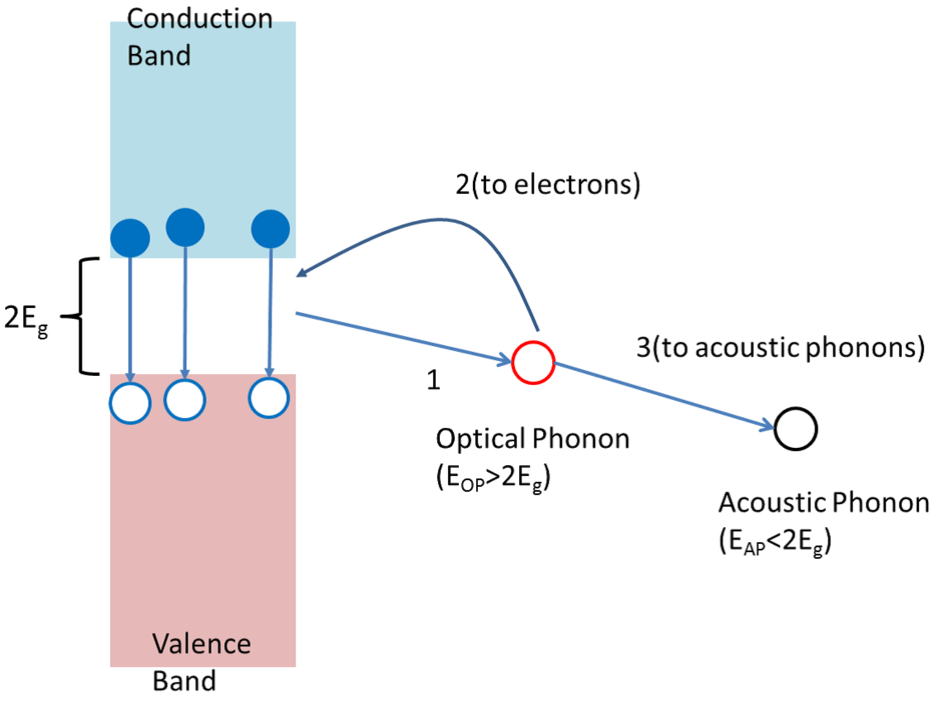

Figure 2.7: A schematic energy flow illustration of single particle decay. Process 1 shows electrons in conduction band give energy to optical phonons and go down valence band. Process 2 shows optical phonons give energy to electrons on valence band and electrons excite to conduction band. Process 3 shows optical phonons give energy to acoustic phonons.

can be applied on the crystal co-axially irrespective of the polarization. The reflection of the pump pulse is cut by color filter. We detect only the reflection of the probe pulse. Time delay between pump and probe pulse is controlled by moving mechanical stage. Two co-axial pulse lasers are applied on the crystal surface at the spot with diameter of 25 μm. The sample stage is cooled down to 10 K by flowing He gas. The temperature is controlled by changing flow rate of He gas.

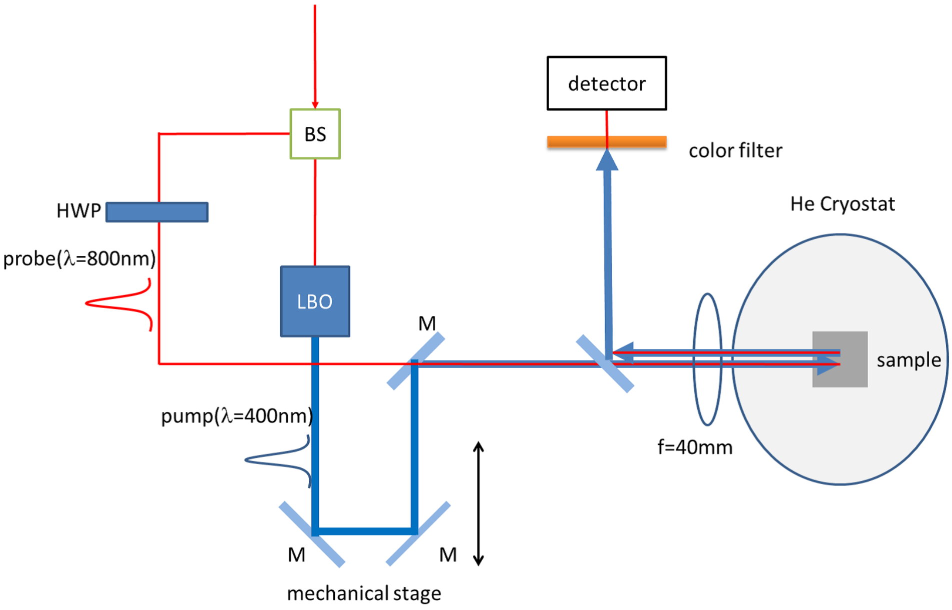

Figure 2.8: A schematic illustration of the two-color pump-probe setup for polarization resolved measurements. The time delay between pump and probe pulse is made by changing optical path length of pump pulse at mechanical stage.

Chapter 3

Results and discussion

3.1 Sample characterization

3.1.1 ICP-AES spectroscopy

Table 3.1 shows the results of ICP-AES spectroscopy on four samples. Sample 1 and 2 are taken from the same ampule. Sample 3 and 4 are taken from the same ampule. Sample 1 and 2 and sample 3 and 4 were made on 600°C and 700°C, respectively. ICP-AES results shows sample 1 and 2 made on 600°C are $Fe_{1.08}Te$ and sample 3 and 4 made on 700°C are $Fe_{1.14}Te$. The amount of excess iron is controllable by growing temperature.

Table 3.1: Results of ICP-AES spectroscopy on several samples.

	Temperature (°C)	Element	element content (mol)	Te:Fe
sample 1	600	Fe	$2.1490*10^{-6}$	1.08231
		Te	$1.9856*10^{-6}$	
sample 2	600	Fe	$4.1979*10^{-6}$	1.08239
		Te	$3.8783*10^{-6}$	
sample 3	700	Fe	$1.5459*10^{-6}$	1.13181
		Te	$1.3659*10^{-6}$	
sample 4	700	Fe	$1.1557*10^{-6}$	1.13856
		Te	$1.0151*10^{-6}$	

3.1.2 Magnetization measurement

Figure 3.1 shows temperature dependence of magnetic susceptibility on $Fe_{1.08}Te$. The magnetic susceptibility decreases with decreasing temperature from 300 K to 68 K. It reduces significantly at 68 K and decreases with decreasing temperature from 68 K. The temperature dependence shows a clear antiferromagnetic transition at 68 K. Figure 3.2 shows temperature dependence of magnetic susceptibility on $Fe_{1.14}Te$. The magnetic susceptibility obeys the Curie-Weiss law above 58 K and then rapidly decreases below 58 K. The temperature dependence shows a clear antiferromagnetic transition at 58 K. Excess irons cause reducing antiferromagnetic transition temperature.

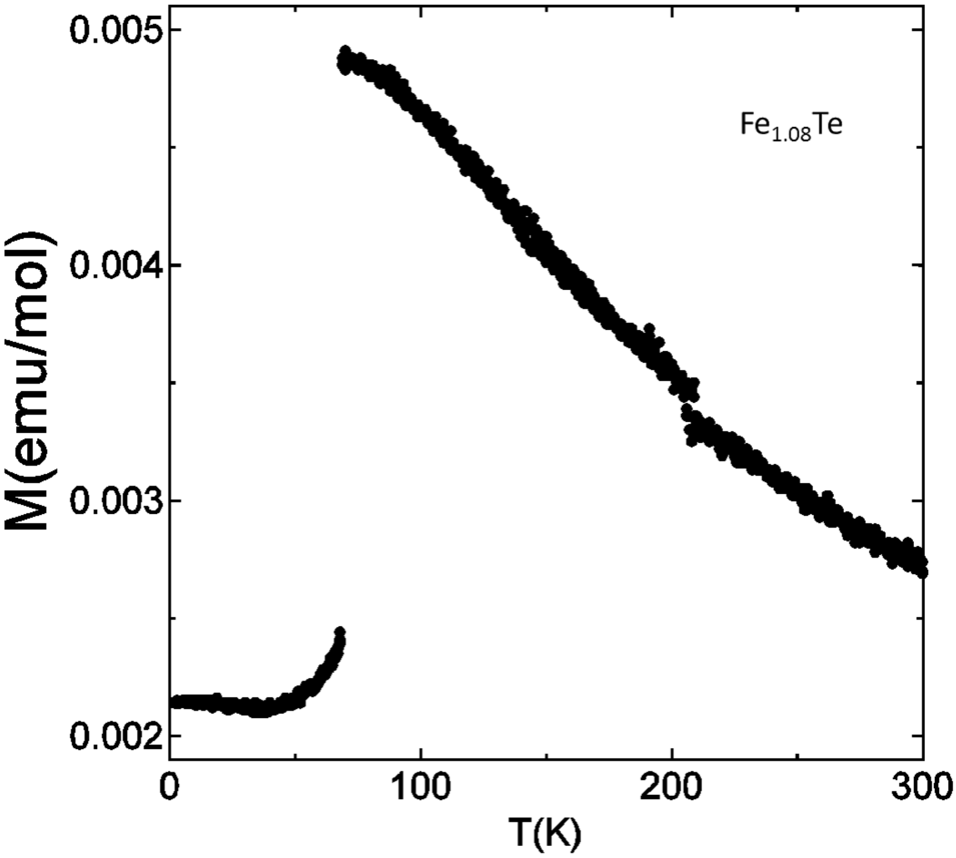

Figure 3.1: Temperature dependence of the magnetic susceptibility on $Fe_{1.08}Te$. There is large reduction of magnetic susceptibility around 68 K. Antiferromagnetic transition temperature is determined as 68 K.

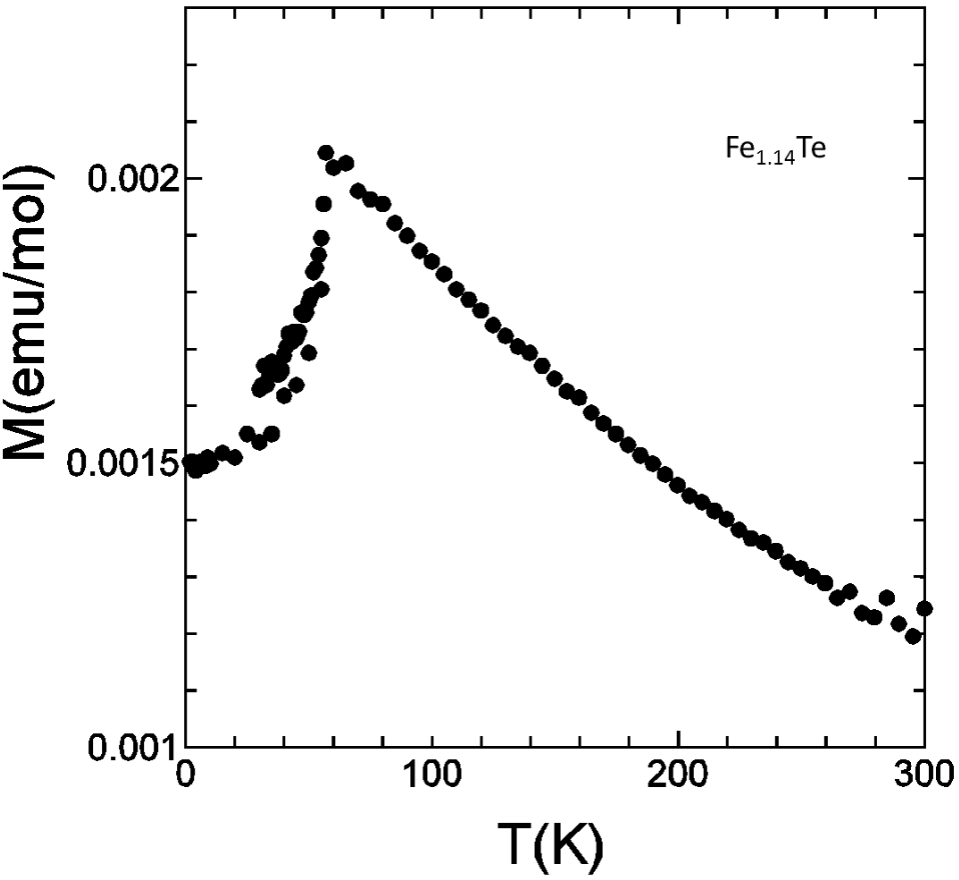

Figure 3.2: Temperature dependence of the magnetic susceptibility on $Fe_{1.14}Te$. There is large reduction of magnetic susceptibility around 58 K. Antiferromagnetic transition temperature is determined as 58 K.

3.1.3 Resistivity measurement

Figure 3.3 shows temperature dependence of resistivity on $Fe_{1.08}Te$. The resistivity increases slightly from 300 K temperature to 65 K with decreasing temperature. The resistivity significantly decreases at 65 K, and then decreases linearly from 65 K to 0.5 K. Figure 3.4 shows temperature dependence of resistivity on $Fe_{1.14}Te$. The resistivity increases slightly from 300 K temperature to 58 K with decreasing temperature. The resistivity exhibits a sharp peak at 58 K, and then it decreases from 58 K to 50 K. The resistivity increases slightly between 50 K and 0.5 K. The slope of the resistivity from 300 K temperature to 58 K is larger than that from 50 K to 0.5 K. Both sample of the temperature dependence of the resistivity over antiferromagnetic transition temperature well fit by the function $\log(T)$. However doping iron does not change the resistivity behavior above transition temperature, the resistivity behavior below transition temperature changes drastically.

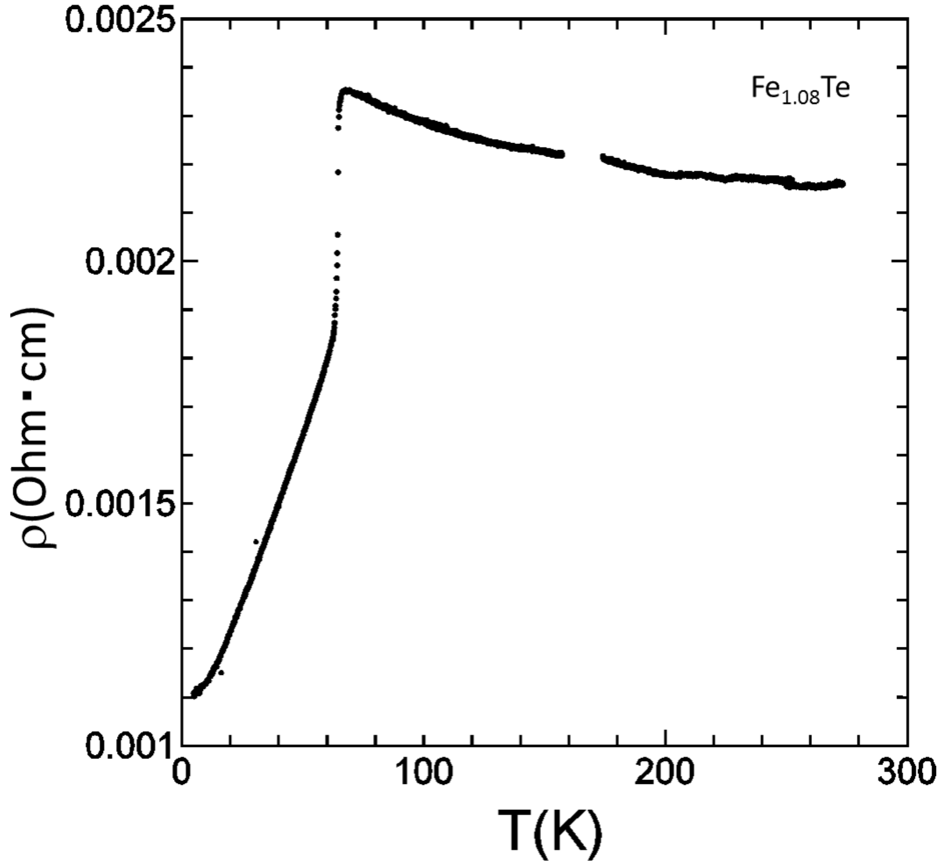

Figure 3.3: Temperature dependence of the resistivity on $Fe_{1.08}Te$.

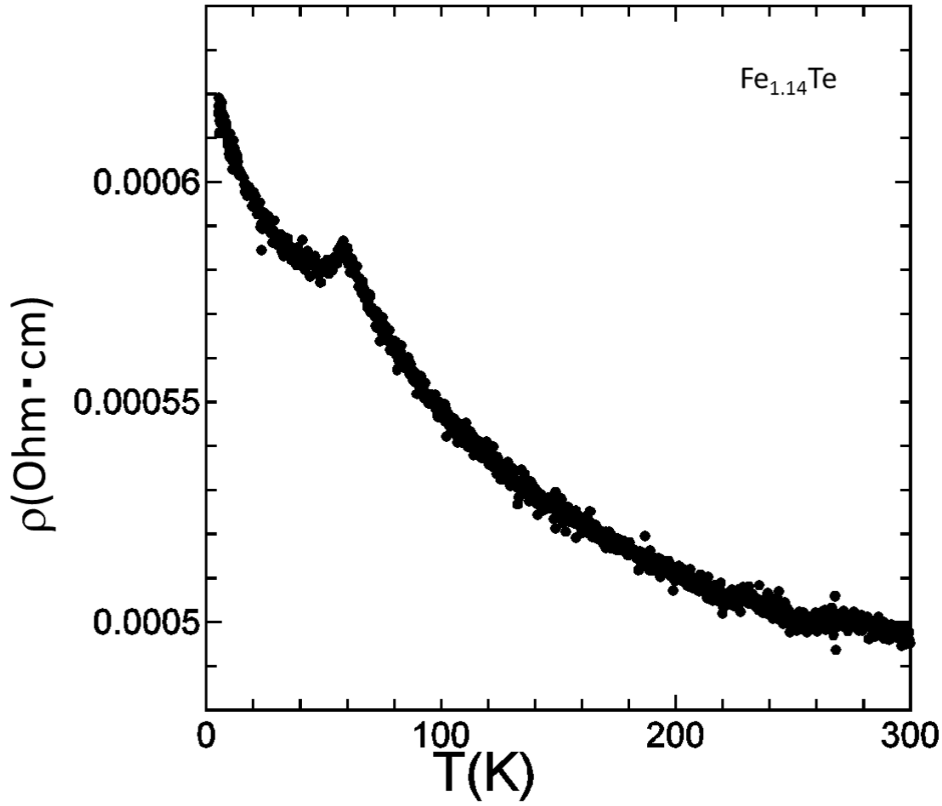

Figure 3.4: Temperature dependence of the resistivity on Fe$_{1.08}$Te.

3.2 STM/STS measurement

3.2.1 STM measurement

Figure 3.5 shows an STM current image of the *a*-*b* surface taken at $T = 80$ K with a bias voltage $V = 1000$ mV and a tunneling current $I = 0.9$ nA. The crystal was cleaved at the *a*-*b* plane as mentioned above. The scanning area of the image is 18×18 nm^2. Atoms are clearly resolved as bright spots, that form a square lattice with sides of 0.38 nm. The length of the lattice side corresponds to a Te lattice on an *a*-*b* layer. The bright spots in Fig. 3.5 indicated by red dots are assigned as Te atoms. I found that the topmost layer was a Te layer resulted from the cleaving. Line A and B on image correspond to line profile A and B, respectively. There are Te atom sharp peaks on both line profiles indicated by red arrows. The clear square lattice observed on 80 K measurement.

I took STM measurement enough low temperature from SDW transition temperature. Figure 3.6 shows an STM current image of the *a*-*b* surface taken at $T = 7.8$ K with a bias voltage $V = 700$ mV and a tunneling current $I = 0.9$ nA. The scanning area of the image is 10×10 nm^2. I discovered the stripe structure in the image. The atoms connect with each other along the Y direction in Fig. 3.6. By contrast, no atoms connect with each other along the X direction in Fig. 3.6. Fig. 3.6 shows electrons make anisotropic structure on FeTe. The bright spots in Fig. 3.6 indicated by red dots are assigned as Te atoms by distance of them. The Te square lattice is same as STM image on 80 K. Taking line profile A and B clear the source of the charge stripe structure. Line profile A shows only Te atoms peaks indicated by red arrows. On the other hands, line profile B shows Te peaks and other peaks indicated by red arrows and blue arrows, respectively. Other peaks may be expected Fe atoms from that positions. These line profile shows obvious anisotropic electron structure which is charge stripe structure on $Fe_{1.14}Te$. I first observed the charge stripe structure for the iron-based superconductor. The charge stripe wave vector direction is along the *a*-axis or *b*-axis of orthogonal crystal. This charge stripe was observed was observed at bias voltage in a range from 50 mV to 1000 mV.

To analyze the stripe structure in detail, I obtained a current image with a small scanning area. Figure 3.7 shows a high-resolution current image obtained at 7.8 K. I took line profiles along lines A, B and C line in Fig. 3.7. Fe atoms beneath a Te layer can be seen in this image. The image was taken at a bias voltage $V = 700$ mV and a tunneling current $I = 1.0$ nA. The image size is 3.3×3.3 nm^2. In the image, there is a stripe structure of which wave vector is parallel to the lines A. The line profile A, which was taken along the blue line in the image, was obtained for both of the direction of the stripe wave vector and on the Te atoms. There are other peaks indicated by blue arrows between the Te peaks in the line profile A. It is likely that the top surface is Te layer as described above. The strong peaks indicated by red arrows correspond to the tunneling current from the Te atoms. The Fe layer is located 0.174 nm below the surface Te layer. I concluded that the weak peaks indicated by blue arrows between the Te peaks were the tunneling current from the Fe layer beneath the Te layer. There are Fe atoms and Te atoms in the image. Line profile B is taken along vertical to the stripe wave vector. There is a tunneling current from the Fe and Te layer in the line profile B. Red and green arrows correspond to Te and Fe atoms, respectively. Line profile A and B show that there is a tunneling current beneath the Fe layer. Fe atoms form a square lattice. The lattice side is 0.27 nm long. The lattice shape is rotated 45 degrees in plane from the Te lattice. These Fe lattice details are consistent with the crystal structure. Line profile C is taken along the side of the Fe lattice. There are two types of tunneling current from the Fe atoms. This result shows that there are two types of Fe site. Each site has a different electronic state. The clear stripe structure is formed of two electronic states on the Fe layer. One is rich in charge and another is poor. I find that the stripe structure is caused by Fe atoms.

3.2.2 STS measurement

Figure 3.8 (a) shows the tunneling differential conductance on $\mathrm{Fe}_{1+x}\mathrm{Te}$ (x=0.14) at 7.8 K and 80 K. At 80 K, the tunneling differential conductance curve is almost flat. At 7.8 K, the conductance curve has a gap structure at ±9 mV indicated by black arrows in Fig. 3.8(a). The tunneling spectra, where the differential conductance at $V = 0$ is well reduced, show a gap structure at the Fermi level. Figure 3.8 (b) shows $\mathrm{d}^2I/\mathrm{d}V^2$ curve which is numerical differential of the differential conductance at 7.8K. The kink positions indicated by black arrow was determined as first peak ($V > 0$) and dip ($V < 0$) in $\mathrm{d}^2I/\mathrm{d}V^2$ curve [41]. I assign the structure at ±9 mV as the SDW gap. It is noteworthy that the shape of the deferential conductance curve on the present material is similar to that of other iron-based superconductors such as the $\mathrm{LaFeAsO}_{1-x}\mathrm{F}_x$[42] and $\mathrm{SmFeAsO}_{1-x}\mathrm{F}_x$ [43]. The existence of the peseudogap is suggested in these materials [42, 43]. In Fig. 3.8, there are kink structure around ±30 mV indicated by green arrows was determined as first dip ($V > 0$) and peak ($V < 0$) in $\mathrm{d}^2I/\mathrm{d}V^2$ curve. The kink structure at ±30 mV is similar to the pseudogap structure observed in other iron-based superconductors [42, 43].

The SDW transition temperature T_{SDW} of 58 K is determined by resistivity and magnetic anomalies. Correspondingly, the $2\Delta_{\mathrm{SDW}}/kT_{\mathrm{SDW}}$ is 3.60 which is almost consistent with the mean field value of 3.52. The gap structure is caused by the SDW transition. I confirmed that the gap structure does not exist at 80 K. This gap structure is an indication of the SDW.

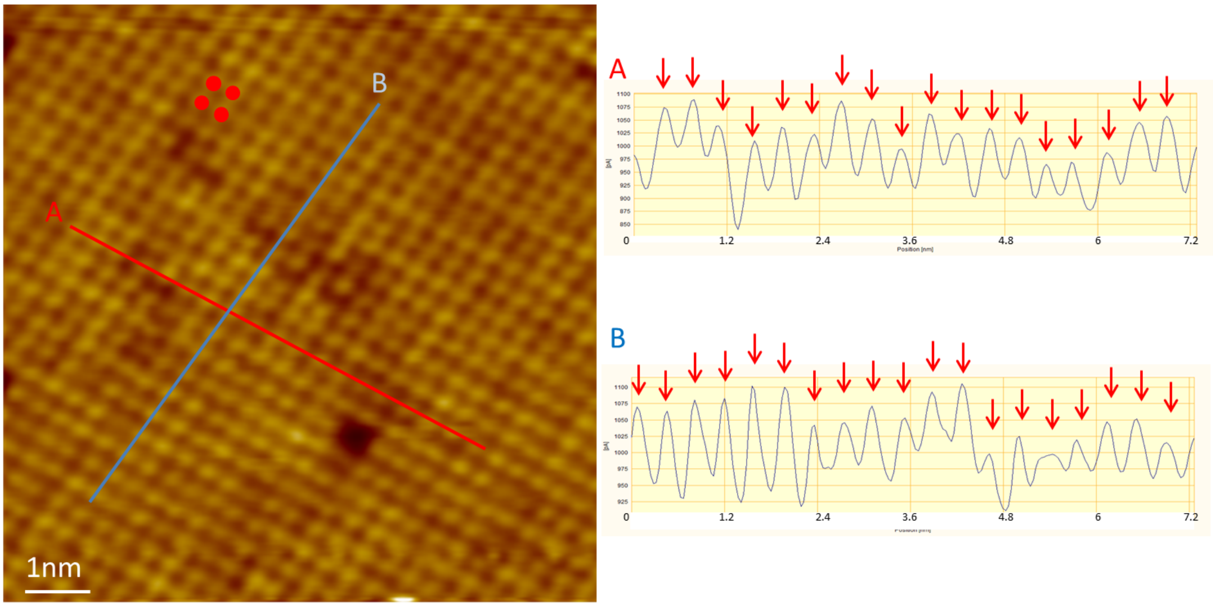

Figure 3.5: STM current image of $Fe_{1+x}Te$ (x=0.14) at bias voltage $V = 1000$ mV and tunneling current $I = 1.0$ nA at 80K. The image size is 18 ×18 nm^2. The red dot shows square lattice Te atoms. Line A and B correspond to line profile A and B, respectively. There are Te atom peaks on both line profiles indicated by red arrows.

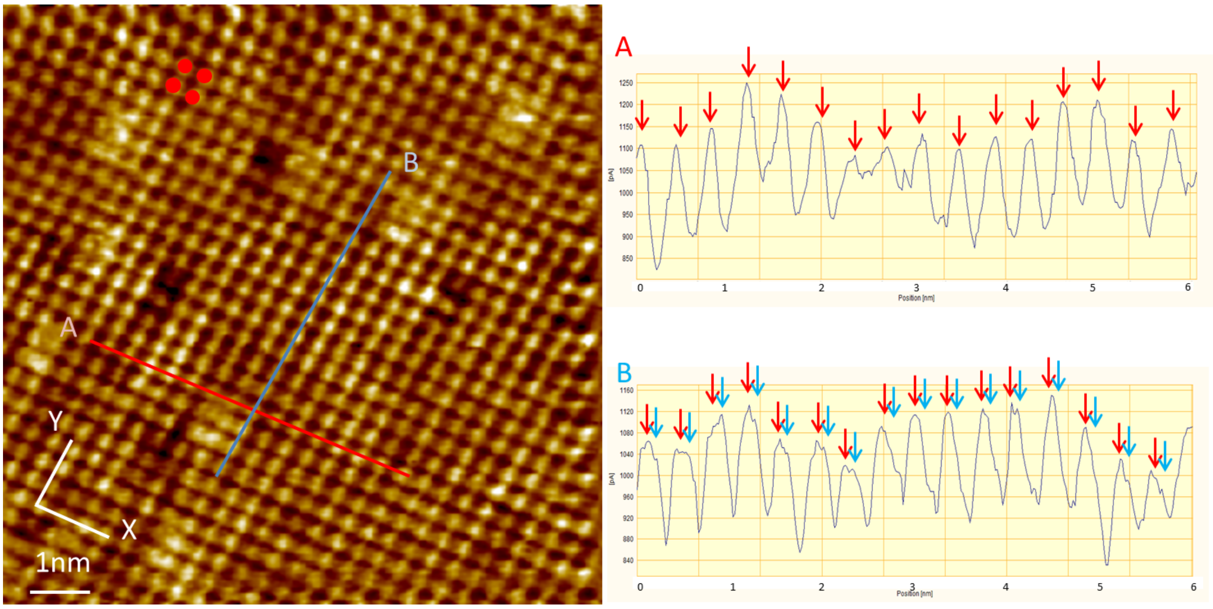

Figure 3.6: STM current image of $Fe_{1+x}Te$ (x=0.14) at bias voltage V = 700 mV and tunneling current I = 1.0 nA. The image size is 10 ×10 nm^2. The red dot shows square lattice Te atoms. Line A and B correspond to line profile A and B, respectively. There Te atom peaks on line profile A indicated by red arrows. There are two peaks on line profile B indicated by red and blue arrows. The peaks indicated by red arrows correspond to Te atoms. The line profiles show anisotropic structure made by charge stripe structure. The charge stripe wave vector is along the X direction. Atoms connect and separate in the Y direction and X directions, respectively.

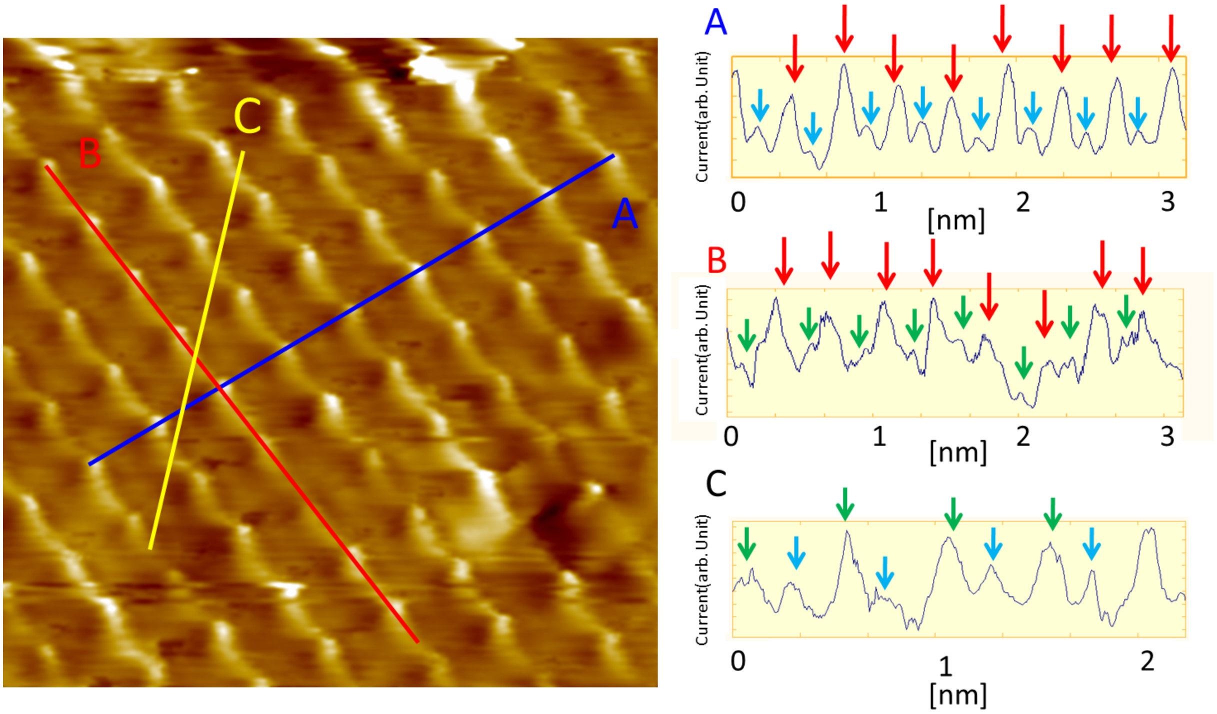

Figure 3.7: STM current image of Fe$_{1+x}$Te (x=0.14) at bias voltage V = 700 mV and tunneling current I = 1.0 nA. The image is 3.3 nm square. There are line profiles in the STM image. A, B and C in the STM image correspond to the line profiles signs. Peaks indicated by green and blue arrows correspond to the tunneling current from Fe atoms. The red arrow peaks correspond to the tunneling current from Te atoms. The kinds of atoms are decided by atomic distance.

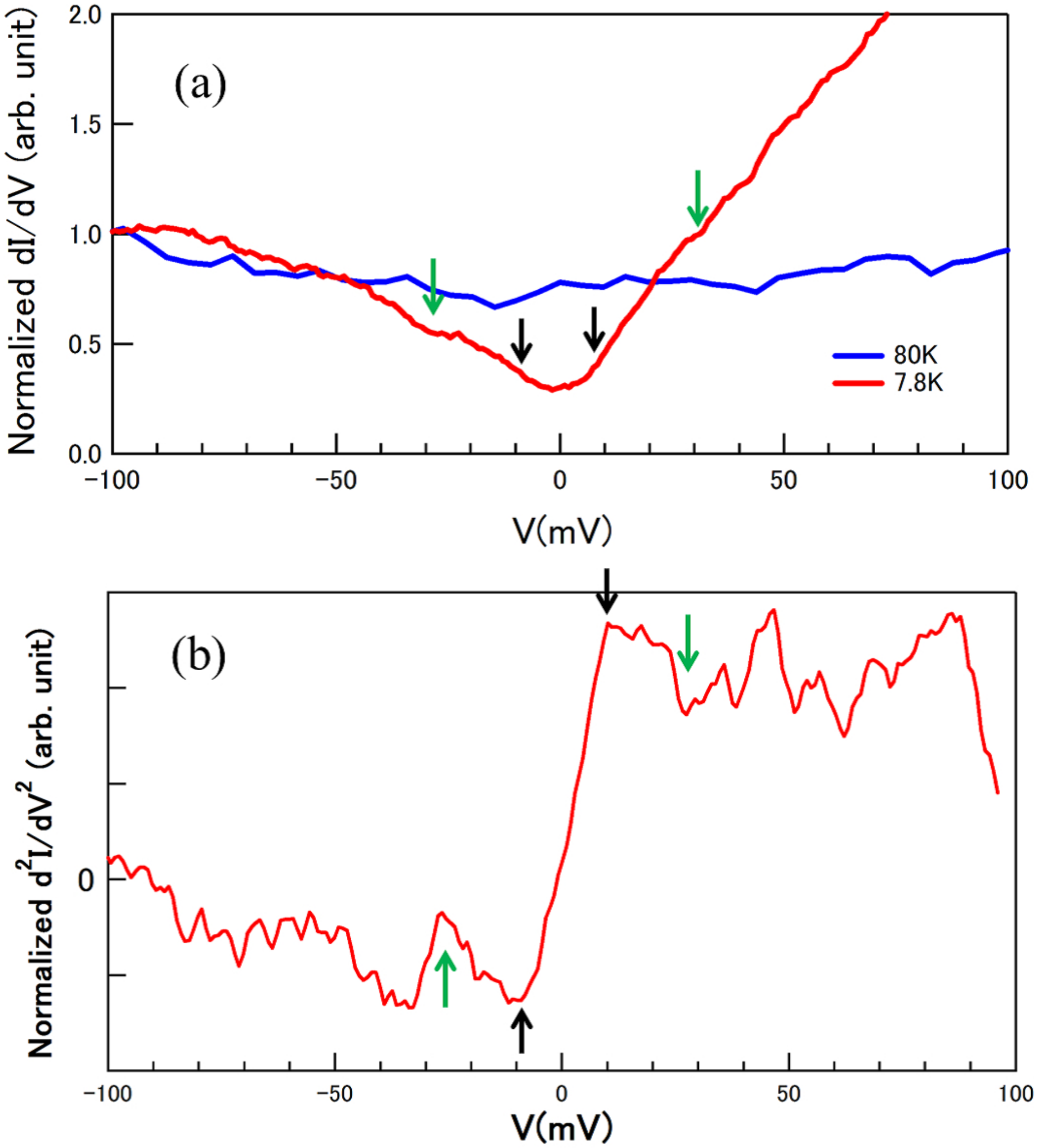

Figure 3.8: (a) Tunneling differential conductance on $Fe_{1+x}Te$ (x=0.14) at 7.8 K and 80K indicated by red and blue line, respectively. Black and green arrows indicate the SDW gap and the pseudogap, respectively. (b) Numerical differential of the differential conductance on $Fe_{1+x}Te$ (x=0.14) at 7.8 K. Black arrows and green arrows correspond to the SDW gap and the pseudogap at the differential conductance curve. $2\Delta_{\mathrm{SDW}}$=18 meV.

3.3 Two color pump-probe time domain reflectivity measurement

3.3.1 $\mathrm{Fe}_{1+x}\mathrm{Te}$ (x=0.14)

Experimental setup

Figure 3.9 shows experimental setup on $\mathrm{Fe}_{1+x}\mathrm{Te}$ (x=0.14). The shape of the sample is rectangle. In $\mathrm{Fe}_{1+x}\mathrm{Te}$, the clean edge of the sample is parallel to the crystal axis. Then the crystal axis was determined from sample shape on Fig. 3.9. The a-axis correspond to the diagonal direction on Fig. 3.9. The angle of 0 degree polarization of the probe pulse set as horizontal on Fig. 3.9.

Temperature dependence of $\Delta R/R$ at 0 degree polarization

Figure 3.10 shows density plot of $\Delta R/R$ transients as a function of temperature on $\mathrm{Fe}_{1+x}\mathrm{Te}$ (x=0.14). The $\Delta R/R$ decrease below 62.5 K corresponding to the antiferromagnetic transition temperature. Decrease of the $\Delta R/R$ seems to assign as SDW transition. SDW transient component was determined by taking single logarithmic plot on 60 K corresponding to SDW transition temperature. Figure 3.11 shows single logarithmic plot of $\Delta R/R$ transients on 60 K. There are three transient components in the $\Delta R/R$ of $\mathrm{Fe}_{1+x}\mathrm{Te}$ (x=0.14). The first is short time exponential decay which has relaxation time about 0.4 ps, the second is long time transient beginning about 2 ps, the third is long-lived back ground component with decay time beyond our measurement.

Figure 3.12 shows $\Delta R/R$ transient curves at several temperatures. At 270 K, there is no short time transient with relaxation time of 0.4 ps. At 70 K, the transient curve has the short relaxation component. From relaxation time of 0.4 ps, this component may correspond to relaxation of nonequilibrium electrons excited by pump pulse. To evaluate the short relaxation component, I plot the difference of $\Delta R/R$ between 0.3 ps and 1 ps as a function of temperature in Fig. 3.14. As shown in the figure, the component with relaxation time of 0.4 ps appears below 170 K and increases with decreasing temperature down to T_{SDW}. The component have maximum at 65 K. The component maximum temperature is near SDW transition temperature from magnetization measurement ($\mathrm{T}_{\mathrm{SDW}}$

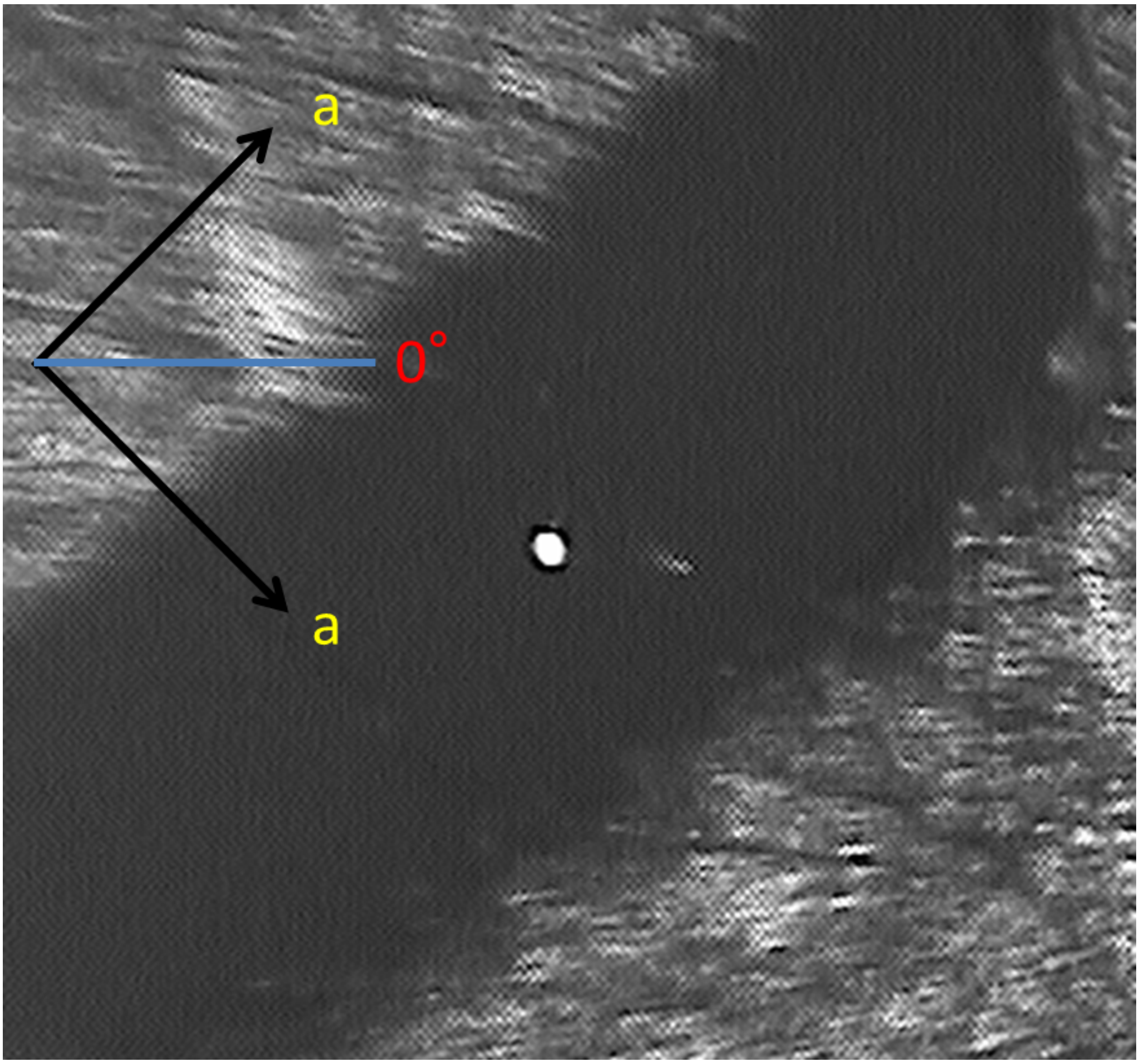

Figure 3.9: Experimental setup at pump probe measurement on $Fe_{1+x}Te$ (x=0.14). Letters a shows crystal axes. The bright white spot correspond to pump probe Laser spot.

= 58 K). Below T_{SDW}, the component decreases with decreasing temperature and vanishes at about 15 K. This component appears above SDW transition temperature and have maximum at SDW transition temperature.

Figure 3.13 shows $\Delta R/R$ transient curves with the semi-log plot to evaluate the long time transient from 2 ps to 15 ps. Curves are normalized at 1 ps. There is no relaxation finishing before 15 ps above 65 K without short time transient which decays before 0.4 ps. At 62.5 K, there is a relaxation starting from 2 ps. Since the temperature is close to T_{SDW}, this relaxation around 2 ps is thought to be associated with the SDW transition. As temperature decreases, the relaxation becomes small and almost vanishes at 10 K. The growing of relaxation from 2 ps to 15 ps can be explained by the developing of the SDW gap, respectively. Then I conclude the transient from 2 ps to 15 ps indicates SDW gap. However the transient from 2ps does not finish at 15ps, we cannot determine the transient time of the SDW gap component. More time scale experiment will determine the temperature dependence of the transient time of the SDW gap component.

There is other relaxation longer than 15 ps which exceeds the time window of present measurements. Figure 3.15 shows temperature dependence of $\Delta R/R$ at 15 ps. It is hard to estimate the relaxation time since the relaxation has much longer time constant than the present time window. However, the long time relaxation component can be evaluate by the plot in Fig. 3.15. $\Delta R/R$ at 15 ps significantly changes at 65 K. The longer time relaxation component changes at the temperature slightly above T_{SDW}.

These three components change significantly around at T_{SDW}. Among these, the relaxation, which starts at 2 ps, appears below T_{SDW}. Therefore, this relaxation corresponds to the formation of the SDW gap.

The temperature dependence of $\Delta R/R$ is supposed to be originated from SDW. Then I tried to estimate the SDW gap from the amplitude of $\Delta R/R$. V. V. Kabanov *et.al.* [44, 45] studied the theoretical analysis of the transient response for electronic states with the narrow energy gap such as CDW and superconducting states. If the temperature dependence of the gap is the BCS type, the excited carrier density is given as,

$$n_{\mathrm{pe}} \propto \frac{1}{\Delta_c(T) + kT/2} \times \frac{1}{1 + g_{\mathrm{ph}}\sqrt{\frac{kT}{\Delta_c(T)}}exp(-\frac{\Delta_c(T)}{kT})} \tag{3.1}$$

where n_{pe} is the excited carrier density and g_{ph} is the coupling constant between quasi particles and phonons. The SDW gap is estimated as a fitting parameter in Eq.(3.1) assuming that the Δ(T) is of the BCS type. The SDW gap is obtained as Δ_{SDW}=17.5 meV, correspondingly $2\Delta_{\mathrm{SDW}}/kT_{\mathrm{SDW}}$=6.54 from the fitting. The obtained value from pump probe measurement is about twice as that obtained from STS. It is concluded that the significant change of the reflectivity is due to the gap forming associated with SDW and not due to the structural transition.

Polarization dependence of the $\Delta R/R$

To analyze the anisotropy of the electronic state in $\mathrm{Fe}_{1+x}\mathrm{Te}$ (x=0.14), polarization dependence was measured. Figure 3.16 shows density plot of $\Delta R/R$ transients as a function of temperature at 0, 45, 90 and 135 polarization. While there are same $\Delta R/R$ transients on each polarizations far above 62.5 K, they are different below 62.5 K. From Fig. 3.16, $\mathrm{Fe}_{1+x}\mathrm{Te}$ (x=0.14) certainly has anisotropic $\Delta R/R$ response in low temperature. While there are anisotropic response on low temperature, $\Delta R/R(T)$ for both 0 and 90 deg polarization has the same temperature dependence. On the other hand, $\Delta R/R(T)$ for 45 and 135 deg polarization differs from that for 0 deg polarization for each. Below T_{SDW}, $\Delta R/R$ for 45 deg polarization is larger and $\Delta R/R$ for 135 deg polarization is smaller than that for 0 deg. Then I extract temperature dependence of $\Delta R/R$ at 0.35 ps of each polarization to look appearing temperature of anisotropy on $\Delta R/R$. Figure 3.17 shows the temperature dependence of $\Delta R/R$ at 0.35 ps for four polarization, 0, 45, 90 and 135 deg. $\Delta R/R$ is identical and has the same temperature dependence irrespective of the polarization for temperature range from 80 K to room temperature as described above. Below T_{SDW}, $\Delta R/R(T)$ has different temperature dependence for each polarization.

Figure 3.18 shows an enlargement of Fig. 3.17 around SDW transition temperature. $\Delta R/R$ does not have the polarization dependence as described above. $\Delta R/R(\mathrm{T})$ slightly differs at 75 K depending on the polarization angle as shown in Fig. 3.18. The anisotropic $\Delta R/R$ response by polarization appears at 75 K. The difference increases with decreasing temperature down to T_{SDW}. Although the difference at 75 K is much smaller than that at T_{SDW}, the polarization dependence is found at 75 K, which is slightly higher than $\mathrm{T}_{\mathrm{SDW}}$. No anomaly was found in the temperature dependence both of the resistivity and magnetic susceptibility. Each of the magnetic and structural transition can not explain this anomaly in the polarization dependence. Therefore, the polarization dependence is thought to be associated with the charge stripe. It is concluded that the charge stripe already appears at 75 K, which is slightly higher than the magnetic and structural transition temperature.

From reflectivity measurements, I reveal the SDW gap associated with the SDW transition and the polarization dependence associated with the charge stripe.

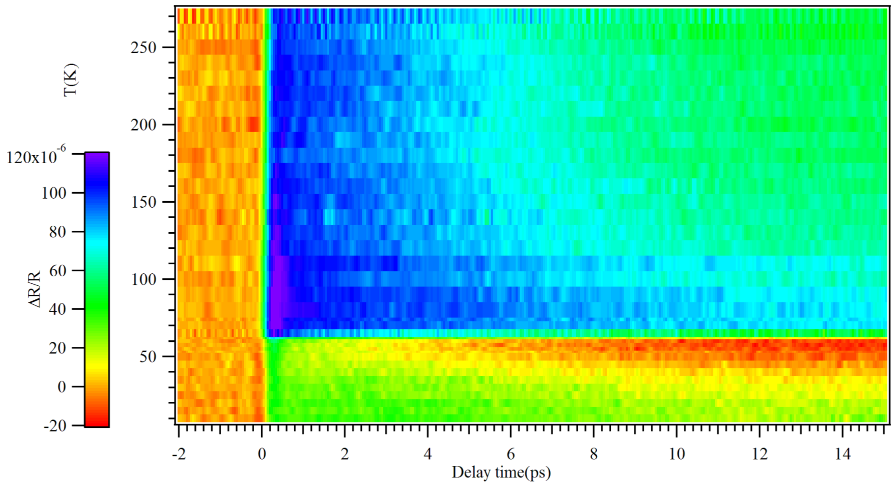

Figure 3.10: Density plot of $\Delta R/R$ transients as a function of temperature at 0 degree polarization at Fig. 3.9.

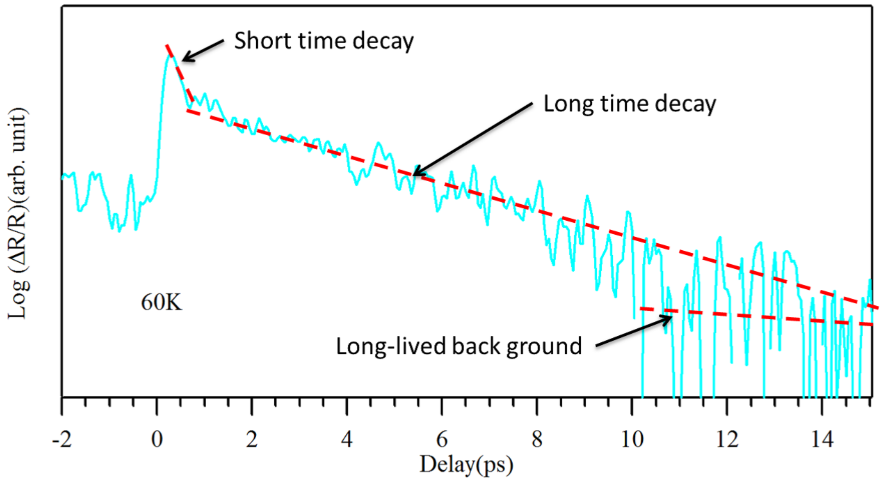

Figure 3.11: Logarithm plot of $\Delta R/R$ at 60 K.

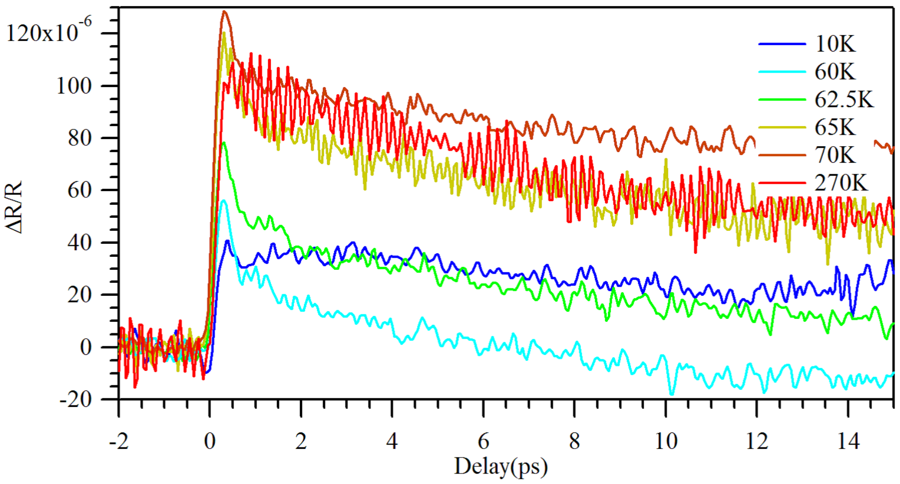

Figure 3.12: $\Delta R/R$ transients at several temperatures from Fig. 3.10.

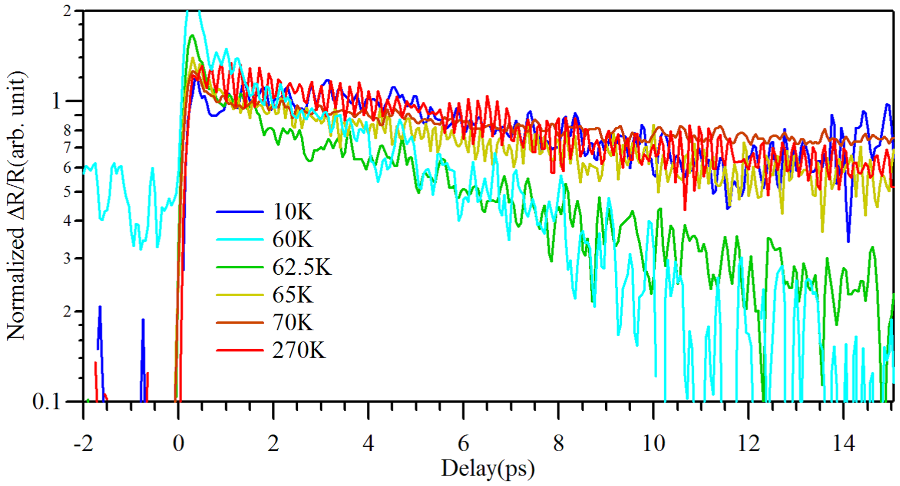

Figure 3.13: Normalized $\Delta R/R$ with the semi-log plot at several temperatures from Fig. 3.10.

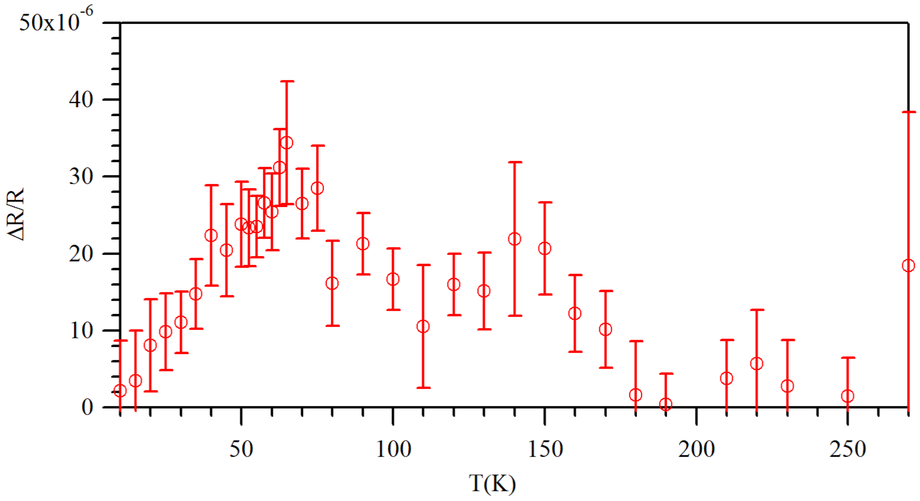

Figure 3.14: Temperature dependence of $\Delta R/R$ difference between the data of 0.3 ps and 1.0 ps.

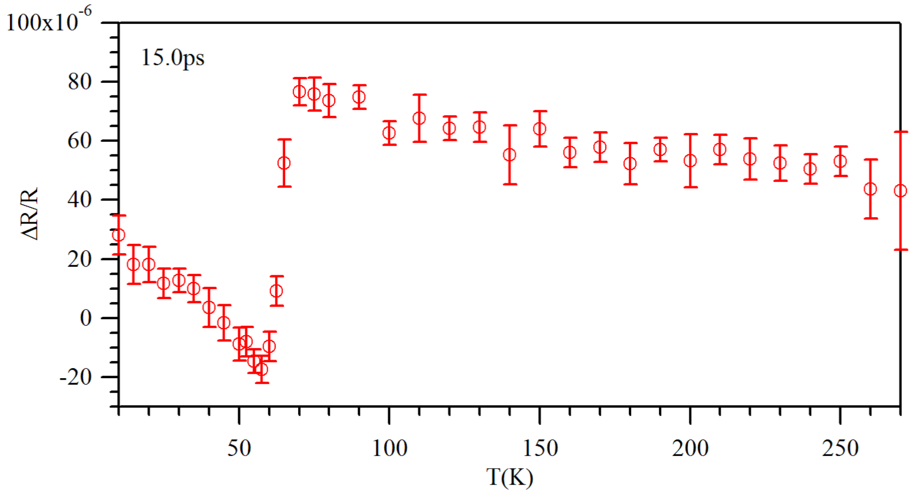

Figure 3.15: Temperature dependence of $\Delta R/R$ at 15.0 ps.

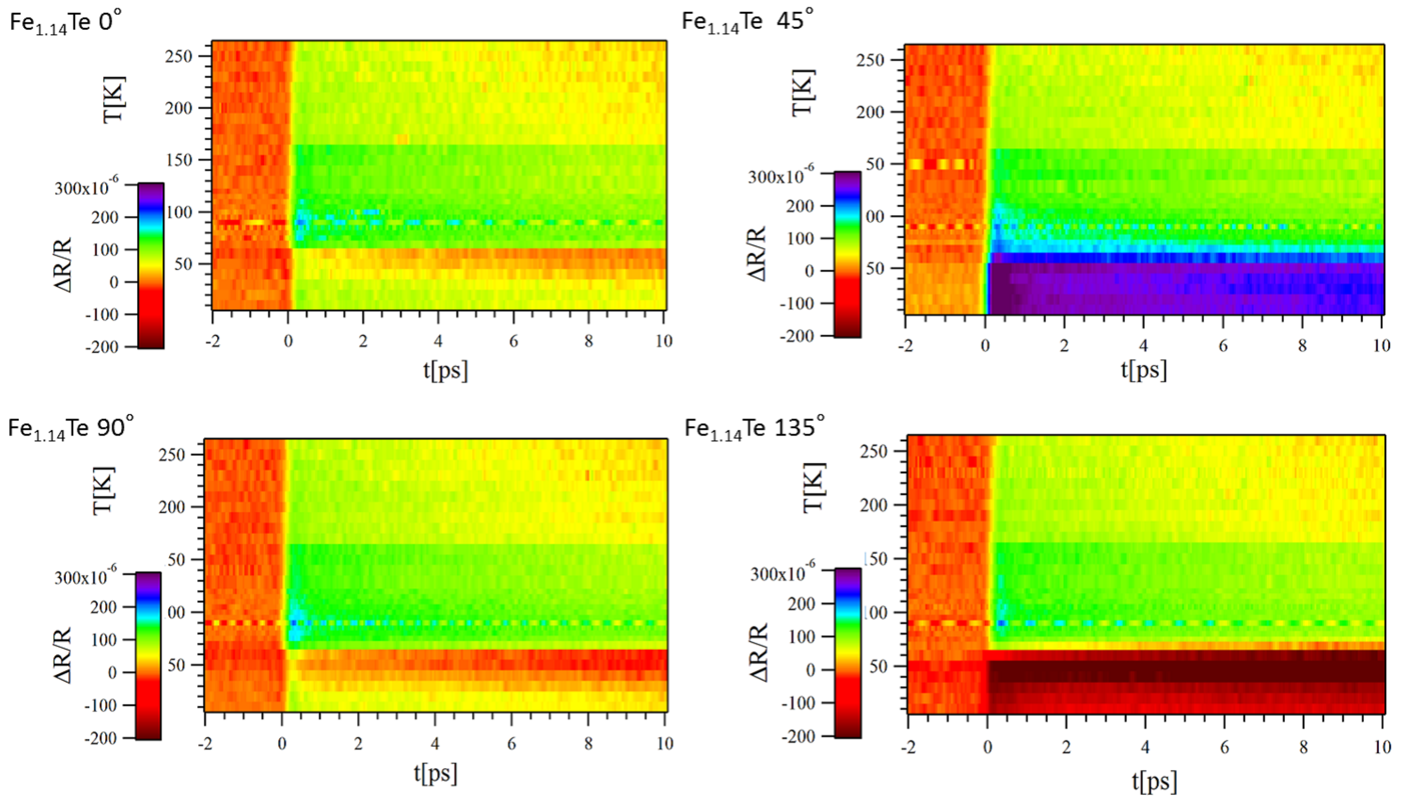

Figure 3.16: Density plot of $\Delta R/R$ transients as a function of temperature at 0, 45, 90 and 135 polarization.

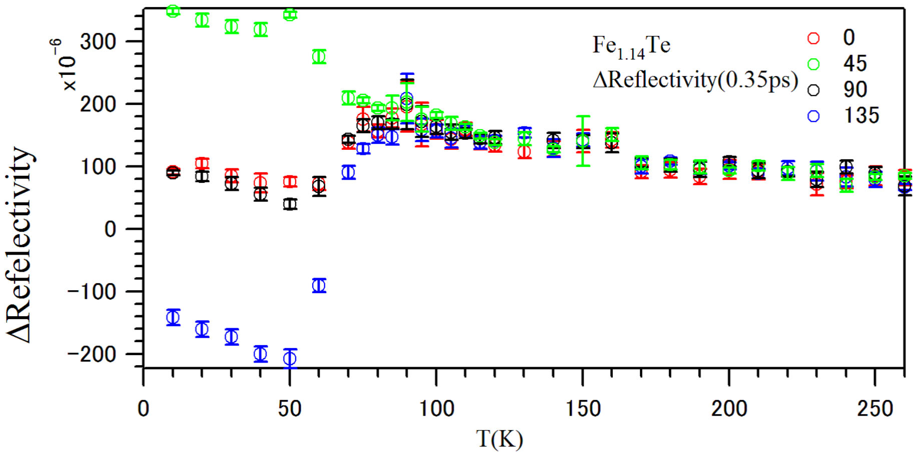

Figure 3.17: Temperature dependence of ΔReflectivity at 0.35 ps at 0, 45, 90 and 135 polarization.

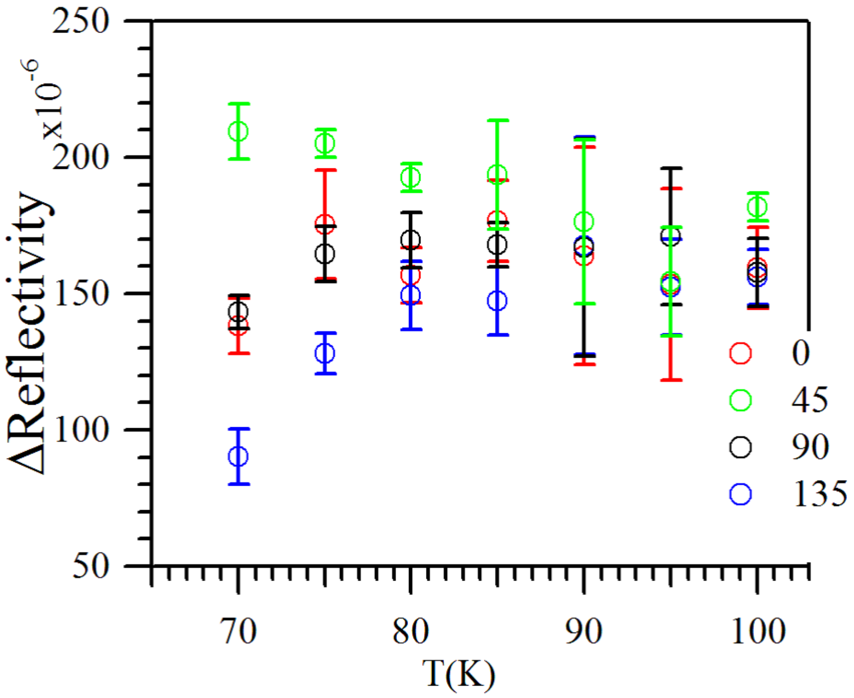

Figure 3.18: Enlargement of Figure 3.17 around SDW transition temperature.

3.3.2 $\mathrm{Fe}_{1+x}\mathrm{Te}$ (x=0.08)

Experimental setup

Figure 3.19 shows experimental setup on $\mathrm{Fe}_{1+x}\mathrm{Te}$ (x=0.08). The shape of the sample is rectangle. In $\mathrm{Fe}_{1+x}\mathrm{Te}$, the clean edge of the sample is parallel to the crystal axis. Then I determine crystal axis from sample shape on Fig. 3.19. a-axis correspond to the diagonal direction on Fig. 3.19 The angle of 0 degree polarization of the probe pulse set as horizontal on Fig. 3.19.

Temperature dependence of $\Delta R/R$

Figure 3.20 shows density plot of $\Delta R/R$ transient as a function of temperature for $\mathrm{Fe}_{1+x}\mathrm{Te}$ (x=0.08). The $\Delta R/R$ transient slightly changes by decreasing temperature from room temperature to 68 K. There are large change on the $\Delta R/R$ transient at 68 K corresponding to SDW transition. Below 68 K, there are no characteristic change down to 10 K which is lowest temperature on the experiment. Figure 3.21 shows $\Delta R/R$ transient curves for $\mathrm{Fe}_{1+x}\mathrm{Te}$ (x=0.08) at several temperatures. As shown in the Fig. 3.21, curves above 68 K are distinguished qualitatively these below 68 K as described above. Temperature dependence of $\Delta R/R$ above 68 K in $\mathrm{Fe}_{1+x}\mathrm{Te}$ (x=0.08) is similar that above 62.5 K in $\mathrm{Fe}_{1+x}\mathrm{Te}$ (x=0.14). Below 68 K, short time transient fall within 1 ps disappears and oscillating component appears. It is difficult to estimate the difference between above and below 68 K after 2 ps from Fig. 3.21. Then semi-log plot of Fig. 3.21 shows in Fig. 3.22. There is a decay range from 2 ps to 12 ps at 66 K on Fig. 3.22. In conclusion, temperature dependence of $\Delta R/R$ transient curves consist of four components. Figure 3.23 and 3.24 shows $\Delta R/R$ transient at 70 K and 66 K, respectively. The short time decay and long-lived back ground component indicate by break line in Fig. 3.23. The oscillating and long time decay component indicate by blue and red circle in Fig. 3.24. Among four components, three components are the same one in the case of $\mathrm{Fe}_{1+x}\mathrm{Te}$ (x=0.14). In that case, the short relaxation with 0.4 ps, the relaxation from 2 ps associated with SDW gap and the long lived relaxation are found as described in Sec. 3.3.1. The short relaxation with 0.4 ps was observed even at 270 K, which is the maximum temperature in the present measurement, although it was observed below 170 K in $\mathrm{Fe}_{1+x}\mathrm{Te}$ (x=0.14).

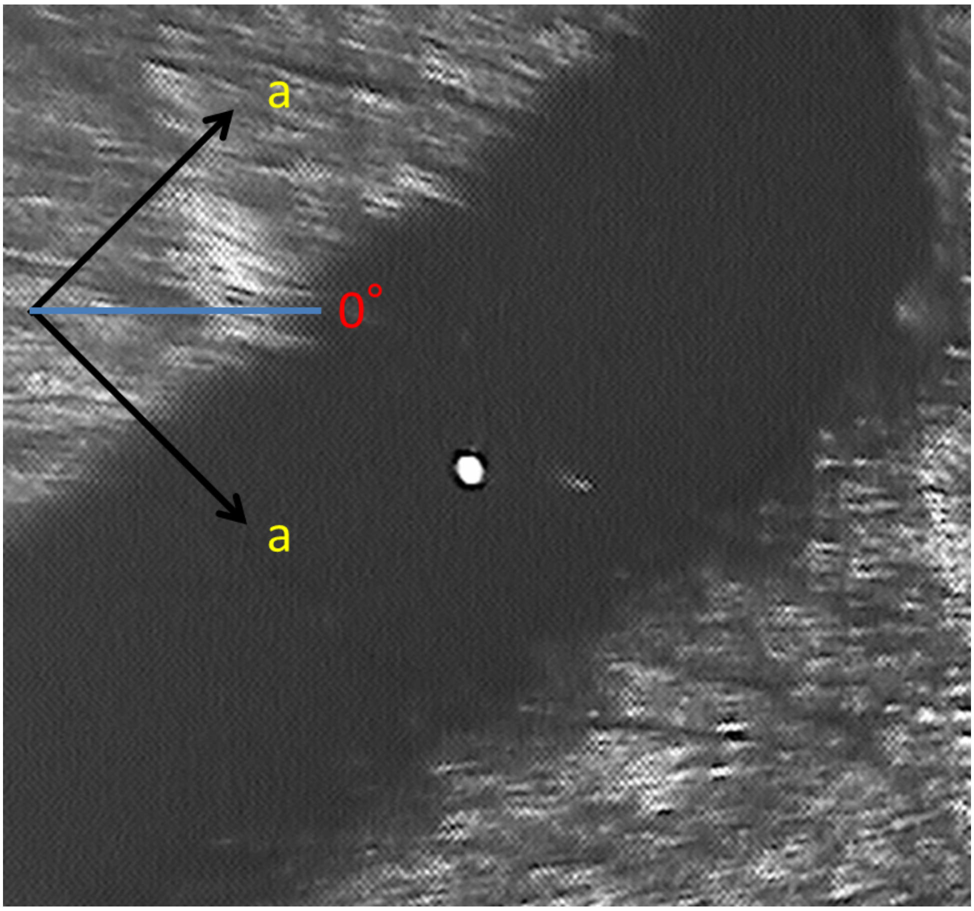

Figure 3.19: Experimental setup at pump-probe measurement on $Fe_{1+x}Te$ (x=0.14). Letters 'a' represents crystal axes. The bright white spot correspond to pump-probe Laser spot.

The short relaxation with 0.4 ps and long lived relaxation components have the same temperature dependence as for $\mathrm{Fe}_{1+x}\mathrm{Te}$ (x=0.14). These components do not change by excess iron doping. Both terms consist from electron-phonon relaxation by these existing temperature and decay times. The short one is non-equilibrium electrons excited by pump pulse relax to optical phonon. The long one corresponds to relax to much lower energy phonon than first one relaxed. The relaxation associated with SDW gap is important in the present discussion. For $\mathrm{Fe}_{1+x}\mathrm{Te}$ (x=0.08), the relaxation from 2 ps appears at 66 K, which is just below SDW transition, as in the case for $\mathrm{Fe}_{1+x}\mathrm{Te}$ (x=0.14). The component decreases with decreasing temperature and vanishes at 10 K. It is concluded that the relaxation from 2 ps is associated with developing of the SDW gap for $\mathrm{Fe}_{1+x}\mathrm{Te}$ (x=0.08) as the same as for $\mathrm{Fe}_{1+x}\mathrm{Te}$ (x=0.14). The SDW transition was successfully revealed by the temperature dependence of $\Delta R/R$ transient both for x=0.08 and 0.14 of $\mathrm{Fe}_{1+x}\mathrm{Te}$. The SDW gap was estimated in the same manner as for $\mathrm{Fe}_{1+x}\mathrm{Te}$ (x=0.14). The SDW gap was obtained as Δ_{SDW}=15 meV from the fitting, correspondingly $2\Delta_{\mathrm{SDW}}/kT_{\mathrm{SDW}}$=5.12.

Unlike the case for $\mathrm{Fe}_{1+x}\mathrm{Te}$ (x=0.14), the oscillation was found in the time range from 0 to 2 ps as shown in Fig. 3.21. From Fig. 3.20, the oscillation has a frequency of 1.67 THz, and its frequency, amplitude and decay time are temperature independent. The origin of the oscillation is thought to be the coherent phonon [40, 46, 47] or coupling with CDW [48]. The coherent phonon is excluded from an origin since its decay time is of a few ten of ps. In the case of the coupling with CDW, the oscillation changes due to the temperature dependence of the CDW formation. As temperature increase, the relaxation should become short and the frequency should increase because of the suppression of CDW. Therefore, a coupling with CDW is also excluded from an origin of the oscillation. The oscillation correspond to temperature independent component which is well known as first order transition like structural transition.

The polarization dependence was found in $\mathrm{Fe}_{1+x}\mathrm{Te}$ (x=0.08) at 10 K as in the case for $\mathrm{Fe}_{1+x}\mathrm{Te}$ (x=0.14). Figure 3.25 shows a polar plot of $\Delta R/R$ at 1 ps as a function of polarization angle for T=10 K and 70 K. $\Delta R/R$ is isotropic at 70 K. At 10 K, which is far below T_{SDW}, the polarization dependence has two-fold symmetry as in the case for $\mathrm{Fe}_{1+x}\mathrm{Te}$ (x=0.14). The anisotropy for $\mathrm{Fe}_{1+x}\mathrm{Te}$ (x=0.08) is much less than that for $\mathrm{Fe}_{1+x}\mathrm{Te}$ (x=0.14).

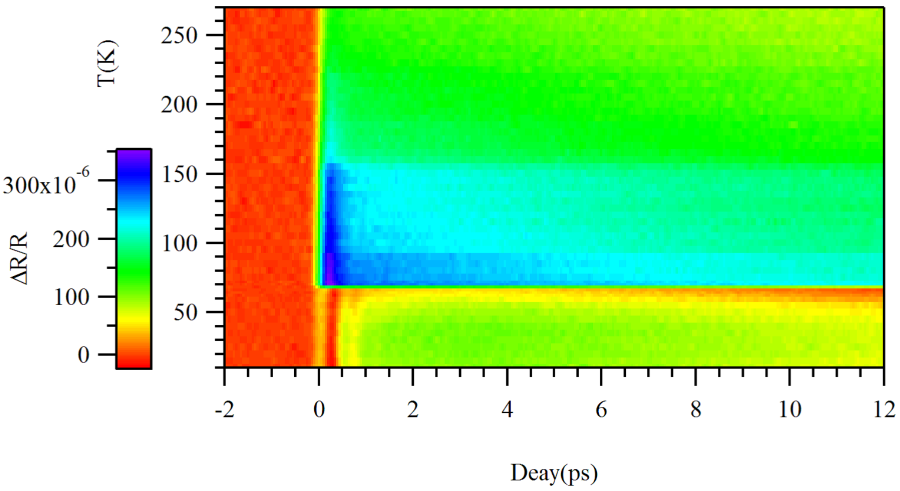

Figure 3.20: Density plot of $\Delta R/R$ transients as a function of temperature.

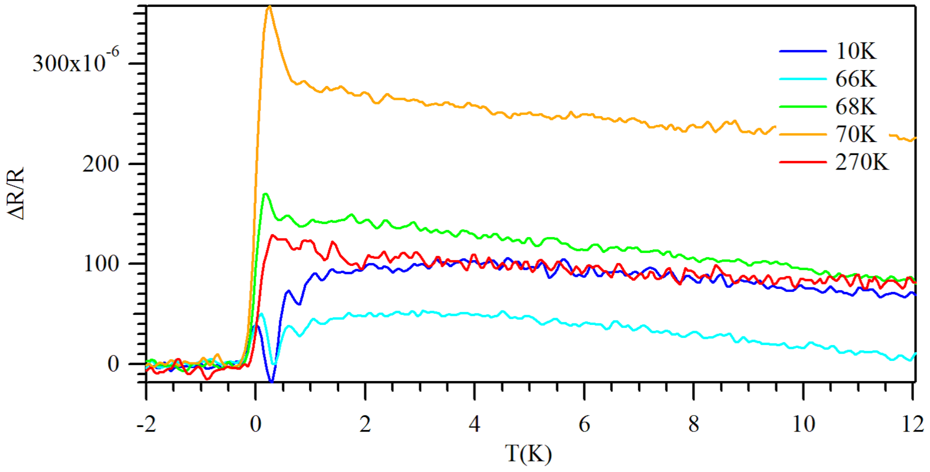

Figure 3.21: $\Delta R/R$ transients at several temperatures from Fig.3.20.

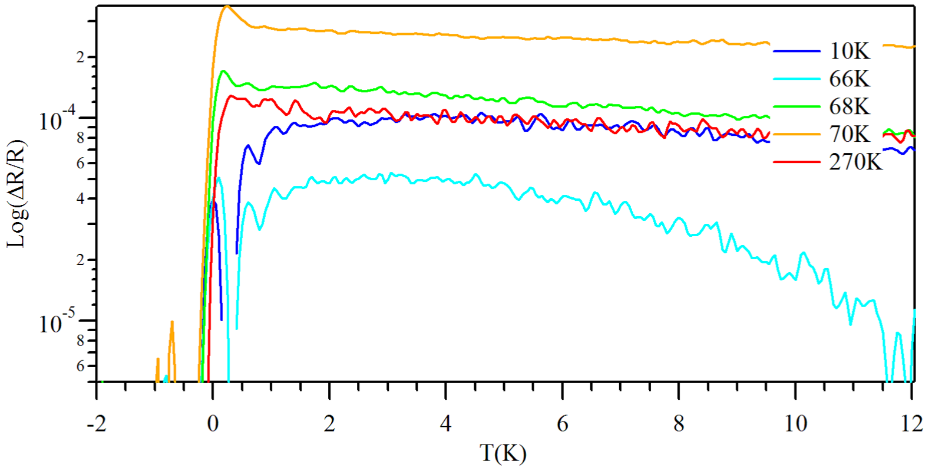

Figure 3.22: Normalized $\Delta R/R$ with the semi-log plot at several temperatures from Fig.3.20.

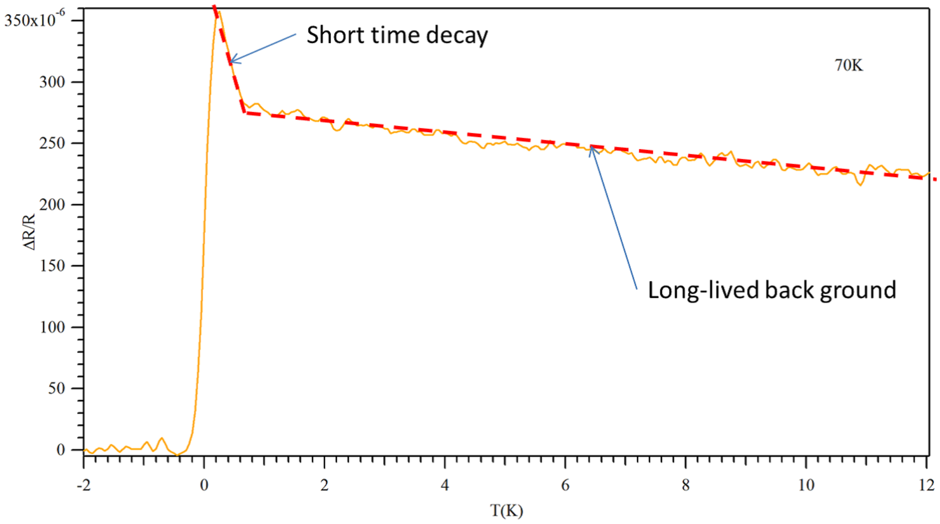

Figure 3.23: $\Delta R/R$ at 70 K.

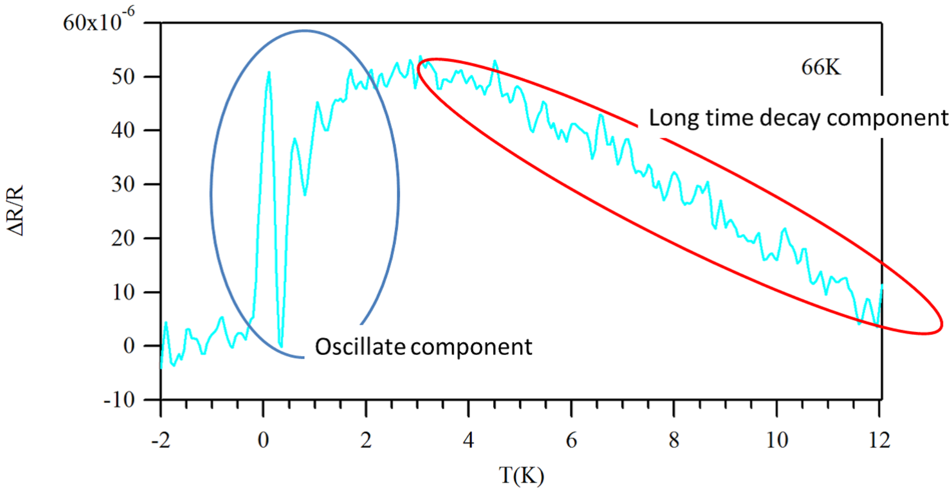

Figure 3.24: $\Delta R/R$ at 66 K.

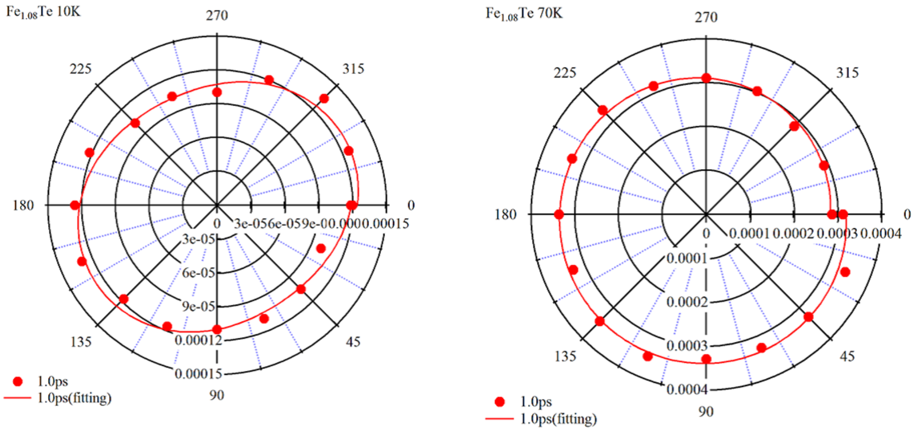

Figure 3.25: Polar plot of $\Delta R/R$ at 10 K and 70 K.

3.3.3 Conclusion of two color pump-probe time domain reflectivity measurement

I performed two color pump-probe time domain reflectivity measurement on $\mathrm{Fe}_{1+x}\mathrm{Te}$ (x=0.08, 0.14). Reflectivity transient associated with SDW transition were observed on both $\mathrm{Fe}_{1+x}\mathrm{Te}$ (x=0.08, 0.14). The estimated SDW gap sizes from temperature dependence of reflectivity are Δ_{SDW}=15 and 17.5 meV for x=0.08 and 0.14, respectively. Anisotropic polarization response was observed on x=0.14. The anisotropy appears at 85 K and increases by decreasing temperature down to 50 K. Temperature where the anisotropy appears is higher than SDW and structural transition temperature. Then I conclude the anisotropy is occurred by charge stripe structure. I observed anisotropic polarization response induced by charge stripe structure. In addition, the anisotropy large increases around SDW transition temperature. This increase supposes to couple SDW and charge stripe structure. On the other hands, x=0.08 does not show anisotropic polarization response, while charge stripe was observed by STM [49, 50]. I think this difference is caused by different crystal and spin structure. The crystal system is orthogonal and tetragonal for $\mathrm{Fe}_{1+x}\mathrm{Te}$ (x=0.14) and $\mathrm{Fe}_{1+x}\mathrm{Te}$ (x=0.08), respectively. The spin structure is spiral SDW (0.35, 0, 1/2) and collinear SDW (1/2, 0, 1/2) on $\mathrm{Fe}_{1+x}\mathrm{Te}$ (x=0.14) and $\mathrm{Fe}_{1+x}\mathrm{Te}$ (x=0.08), respectively. The reflectivity is effected by the electronic density of states changed by crystal structure and spin structure. Then the temperature dependence of reflectivity has a possibility of changing by crystal structure and spin structure changing. The reflectivity on $\mathrm{Fe}_{1+x}\mathrm{Te}$ (x=0.08) is dominated by these changing and does not have so much anisotropic component caused by charge stripe such as $\mathrm{Fe}_{1+x}\mathrm{Te}$ (x=0.14).

3.4 Classify of the charge stripe structure

Figure 3.26 shows classification of charge stripe distinguished by mother material and crystal symmetry. Mother material of Mott insulators are insulating. Because it has strong on-site coulomb interaction. On the other hands, in iron-based superconductors, the coulomb interaction is comparable to the transferring energy. Actually, there is no insulating phase in phase diagram of iron-based superconductors. The crystal symmetries of organic conductors are low. Because donor Molecular of organic conductors have tabular structure, making high symmetric electron structure on organic conductor is very difficult. Arrangements of donor molecular make various ground states including charge order. The charge order is governed by the anisotropy of electronic structure made by anisotropic donor molecular and its arrangement. Mott insulator materials and iron-based superconductors have tetragonal crystal structure. Tetragonal crystal structure means 4-fold rotational symmetry in some plane, while Charge stripe structure has 2-fold rotational symmetry. Then crystal symmetry is higher than the symmetry of charge stripe on Mott insulator and iron-based superconductors. The viewpoints of mother material and crystal symmetry classify charge stripe in organic conductors, Mott insulators and iron-based superconductors. It is note worthy that charge stripe on iron-base superconductors is new type of charge stripe. Then we need consider new mechanism of the charge stripe in iron-based superconductors.

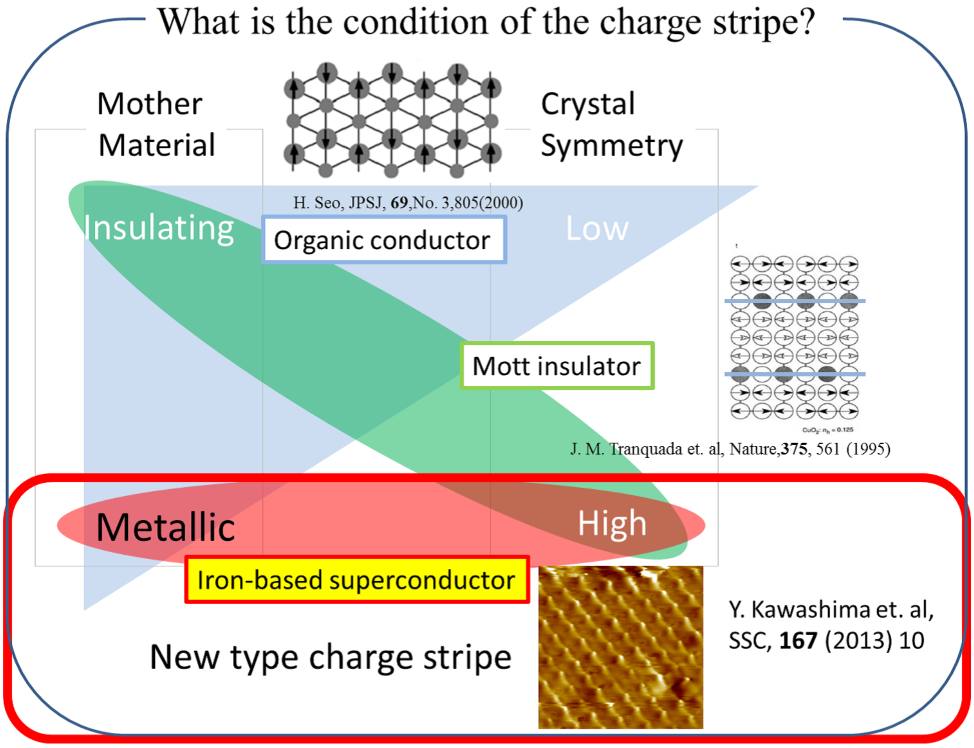

Figure 3.26: The classification diagram of charge stripe distinguished by mother material and crystal symmetry.

Chapter 4

Conclusion

STM measurement on $\mathrm{Fe}_{1+x}\mathrm{Te}$ (x=0.14) was performed. I discovered charge stripe structure in $\mathrm{Fe}_{1+x}\mathrm{Te}$ (x=0.14) on 8 K by STM measurement. The stripe structure is formed of two electronic states on the Fe layer. I observed SDW gap and pseudogap structure in STS measurement. The SDW gap size was assigned as ±9 mV. The $2\Delta_{\mathrm{SDW}}/kT_{\mathrm{SDW}}$ is 3.60 which is almost consistent with the mean field value of 3.52. The pseudogap structure appears around ±30 mV.

I measured reflectivity of excited electron state by femtosecond time-resolved reflection measurements on $\mathrm{Fe}_{1+x}\mathrm{Te}$ (x=0.08 and 1.14). Anisotropic polarization dependence of reflectivity transient was observed below 75 K on $\mathrm{Fe}_{1+x}\mathrm{Te}$ (x=0.14). Temperature, where the polarization anisotropy appears, is different from SDW transition temperature. Then I conclude this anisotropy comes from the charge stripe structure. Reflectivity transient by SDW gap construction and growing was observed. The SDW gap size is estimated as 17.5 meV by temperature dependence of transient. The $2\Delta_{\mathrm{SDW}}/kT_{\mathrm{SDW}}$ is 6.54. There is isotropic polarization reflectivity transient by SDW gap in $\mathrm{Fe}_{1+x}\mathrm{Te}$ (x=0.08). The SDW gap size is estimated at 15 meV by temperature dependence of reflectivity transient. Correspondingly, The $2\Delta_{\mathrm{SDW}}/kT_{\mathrm{SDW}}$ is 5.11.

I discovered new type of charge stripe structure by STM and its anisotropic reflectivity by pump-probe measurement.

Results of both studies of STM and time-domain reflectivity for $\mathrm{Fe}_{1+x}\mathrm{Te}$ are summarized in Table 4.1. The charge stripe structure was found both for x=0.08 and 0.14 at low temperature by STM measurements. T. Machida *et.al.* [49] and M. Enayat *et.al.* [50]

reported that the charge stripe has a wave number along a*. Anisotropy of reflectivity was found in the present study on $\mathrm{Fe}_{1+x}\mathrm{Te}$ (x=0.14), and is associated with the charge stripe. In $\mathrm{Fe}_{1+x}\mathrm{Te}$ (x=0.08), on the other hand, the polarization dependence was observed only at 10 K far below T_{SDW} and the anisotropy is much smaller than that for $\mathrm{Fe}_{1+x}\mathrm{Te}$ (x=0.14). This difference shows $\mathrm{Fe}_{1+x}\mathrm{Te}$ (x=0.14) and $\mathrm{Fe}_{1+x}\mathrm{Te}$ (x=0.08) have large difference on reflectivity response. The reflectivity response is effected by not only electronic state but also crystal structure. The crystal structure of $\mathrm{Fe}_{1+x}\mathrm{Te}$ (x=0.14) and $\mathrm{Fe}_{1+x}\mathrm{Te}$ (x=0.08) are orthogonal and monoclinic, respectively. The SDW spin structure of $\mathrm{Fe}_{1+x}\mathrm{Te}$ (x=0.14) and $\mathrm{Fe}_{1+x}\mathrm{Te}$ (x=0.08) are spiral SDW and collinear SDW, respectively. These differences effect to reflectivity response and make disappearance of anisotropic polarization signal on $\mathrm{Fe}_{1+x}\mathrm{Te}$ (x=0.08). I realize $\mathrm{Fe}_{1+x}\mathrm{Te}$ (x=0.14) and $\mathrm{Fe}_{1+x}\mathrm{Te}$ (x=0.08) is different material from view point of reflectivity.

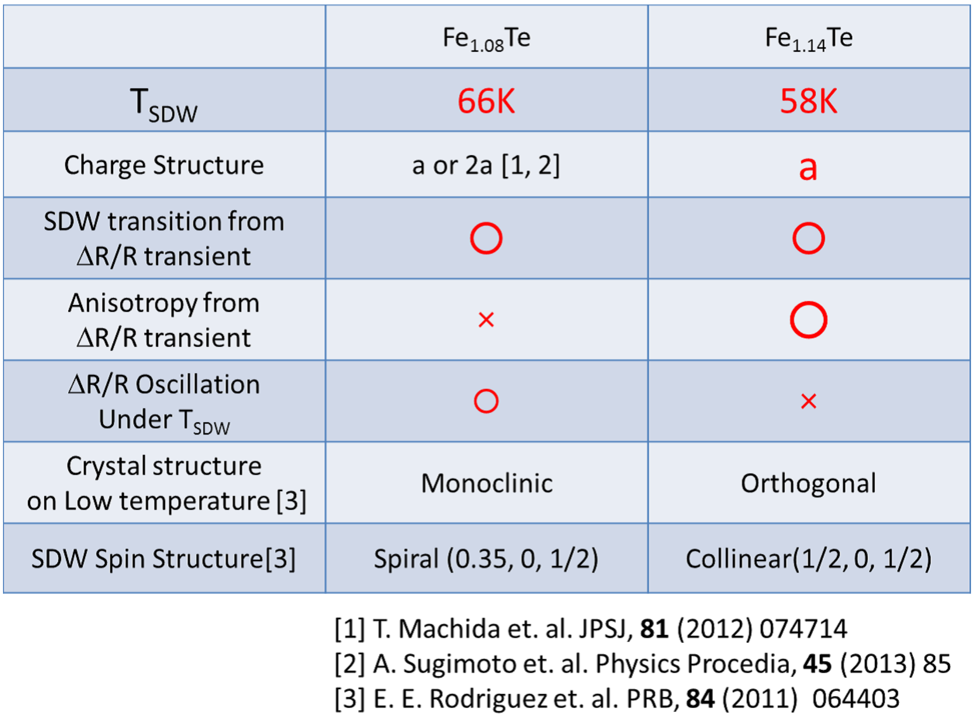

	$Fe_{1.08}Te$	$Fe_{1.14}Te$
T_{SDW}	66K	58K
Charge Structure	a or 2a [1, 2]	a
SDW transition from ΔR/R transient	○	○
Anisotropy from ΔR/R transient	×	○
ΔR/R Oscillation Under T_{SDW}	○	×
Crystal structure on Low temperature [3]	Monoclinic	Orthogonal
SDW Spin Structure[3]	Spiral (0.35, 0, 1/2)	Collinear(1/2, 0, 1/2)

[1] T. Machida et. al. JPSJ, **81** (2012) 074714
[2] A. Sugimoto et. al. Physics Procedia, **45** (2013) 85
[3] E. E. Rodriguez et. al. PRB, **84** (2011) 064403

Figure 4.1: Collection of Experimental results on $Fe_{1+x}Te$ (x=0.08 and 0.14) from STM [49, 50], neutron powder diffraction [51] and time domain reflectivity measurement. We performed red letter part experiments.

Acknowledgments

There are many people who I would like to thank for their support during my life at Hokkaido University. I would like to express my deep gratitude to my supervisor, Prof. K. Ichimura. His wide knowledge and his logical way of thinking have been great value for me.

I would like to thank to Prof. S. Tanda of Hokkaido University for helpful advice and interesting idea of topological science. I would like to acknowledge to Prof. M. Oda and Assistant Prof. T. Kurosawa of Hokkaido University for STM measurement and fruitful discussion. I would like to acknowledge to Prof. Y. Toda of Hokkaido University for optical measurement and discussions. I would like to thank to Prof. K. Yamaya and Prof. S. Takayanagi of Hokkaido University for helpful instructions of low temperature resistivity measurement and making crystals. I would like to thank to Assistant Prof. T. Matuura of Hokkaido University for helpful instructions of low temperature resistivity measurement. I would like to acknowledge to Prof. H. Hosono of Tokyo Institute of Technology, Prof. H. Takahashi of Nihon University and Associate Prof. Y. Kamihara of Keio University for giving me valuable samples of iron-based superconductors. I would like to acknowledge Dr. J. Ishioka and Dr. M. Tsubota of Hokkaido University for helpful instructions about observation of samples by FE-SEM and TEM. I would like to thank for members of laboratory of topological science and technology and high pressure physics laboratory of department of physics for daily supports and encouragements.

References

[1] Stephen A. Langer and James P. Setha, Phys. Rev. A **34** (1986) 5035.

[2] Shuji Sudo, Katuya Mituoka, Kazuyuki Koike, Hideo Matsuyama and Yutaka Sugita, Jpn. J. Appl. Phys. **33** (1994) L30.

[3] G. Malescio and G. Pellicane, Nature Materials **2** (2003) 97.

[4] E. Winger, Phys. Rev. **46** (1934) 1002.

[5] T. Takahashi, Y. Nogami and K. Yakushi, J. Phys. Soc. Jpn. **75** (2006) 051008–1.

[6] H. Seo J. Phys. Soc. Jpn. **69** (2000) 805.

[7] J. Zaanen and O. Gunnarsson, Phys. Rev. B **40** (1989) 7391.

[8] J. M. Tranquada, B. J. Sternlleb, J. D. Axe, Y. Nakayama and S. Uchida, Nature **375** (1995) 561.

[9] C. Howald, H. Eisaki, N. Kaneko, M. Greven and A. Kapitulnik, Phys. Rev. B **67** (2003) 014533–1.

[10] J. M. Tranquada, D. J. Buttrey, V. Sachan and J. E. Lorenzo, Phys. Rev. Lett. **73** (1994) 1003.

[11] C. H. Chen, S-W. Cheong and H. Y. Hwang, J. Appl. Phys. **81** (1997) 4326.

[12] C. Renner, G. Aeppil, B.-G. Klm, Y.-A. Soh and S.-W. Cheong, Nature **416** (2002) 518.

[13] A. T. Boothroyd, P. Babkevich, D. Prabhakaran and P. G. Freeman, Nature **471** (2011) 341.

[14] J. M. Tranquada, D.J. Buttrey and V. Sachan, Phys. Rev. B **54** (1986) 12318.

[15] P. Wochner, J. M. Tranquada, D. J. Buttrey and V. Sachan, Phys. Rev. B **57** (1998) 1066.

[16] H. Yoshizawa, T. Kakeshita, R. Kajimoto T. Tanabe, T. Katsufuji and Y. Tokura, Pyhs. Rev. B **61** (2000) R854.

[17] K. Ishizaka, Y. Taguchi, R.Kajimoto, H. Yoshizawa and Y. Tokura, Phys. Rev. B **67** (2003) 184418-1.

[18] Y. Kamihara, H. Hiramatsu, M. Hirano, R. Kawamura, H. Yanagi, T. Kamiyama and H. Hosono, J. Am. Chem. Soc. **128** (2006) 10012.

[19] Y. Kamihara, T. Watanabe, M. Hirano and H. Hosono, J. Am. Chem. Soc. **130** (2008) 3296.

[20] M. Rotter, M. Tegel and D. Johrendt, Phys. Rev. Lett. **101** (2008) 107006–1.

[21] J. H. Tapp, Z. Tang, B. Lv, K. Sasmal, B. Lorenz, P. C. W. Chu and A. M. Guloy, Phys. Rev. B **78** (2008) 060505–1.

[22] F.-C. Hsu, J.-Y. Luo, K.-W. Yeh, T.-K. Chen, T.-W. Huang, P. M. Wu, Y.-C. Lee, Y.-L. Huang, Y.-Y. Chu, D.-C. Yan and M.-K. Wu, Proc. Natl. Acad. Sci. U.S.A. **105** (2011) 14262.

[23] M. H. Chen, T. Wu, G. We, R. H. Liu, H. Chen and D. F. Fang, Nature **453** (2008) 761.

[24] Z.-A. Ren, J. Yang, W. Lu, W. Yi, X.-L. Shen, Z.-C. Li, G.-C. Che, X.-L. Dong, F. Zhou and Z.-X. Zhao, Europhys. Lett. **82** (2008) 57002p1.

[25] E. P. Khlybov, O. E. Omelyanovsky, A. Zaleski, A. V. Sadakov, D. R. Gizatulin, L. F. Kulikova, I. E. Kostuleva and V. M. Pudalov, J. Exp. Theor. Phys. **90** (2009) 387.

[26] S. Iimura, S. Matsuishi, H. Sato, T. Hanna, Y. Muraba, S. W. Kim, J. Eun Kim, M. Takata, and H. Hosono, Nature Comm. **3** (2013) 943 .

[27] M. Rotter, M. Tegel, D. Johrendt, I. Schellenberg, W. Hermes and R. Pottgen, Phys. Rev. B **78** (2008) 020503–1.

[28] M. Yi, D. H. Lu, J. G. Analytis, J. -H. Chu, S. -K Mo, R. -H. He, M. Hashimoto, R. G. Moore, I. I. Mazin, D. J. Singh, Z. Hussain, I. R. Fisher and Z. -X. Shen, Phys. Rev. B **80** (2009) 174510.

[29] A. Subedi, L. Zhang, D. J. Singh and M. H. Du, Phys. Rev. B **78** (2008) 134514.

[30] K. Mortensen, Y. Tomkiewicz and K. Bechgaard, Phys. Rev. B **25** (1982) 3319.

[31] K. Nomura. T. Shimizu, K. Ichimura, T. Sambongi, M. Tokumoto, H. Anzai and N. Kinoshita, Solid. State. Comm. **72** (1989) 1123.

[32] G. Kriza, G. Quirion, O. Traetteberg, W. Kang and D. Jerome, Phys. Rev. Lett. **66** (1991) 1922.

[33] Y. Xia, D. Qian, L. Wray, D. Hsieh, G. F. Chen, J. L. Luo, N. L. Wang and M. Z. Hasan, Phys. Rew. Lett. **103** (2009) 037002–1.

[34] H. Chen, Y. Ren, Y. Qiu, W. Bao, R. H. Liu, G. Wu, T. Wu, Y. L. Xie, X. F. Wang, Q. Huang and X. H. Chen, Europhys. Lett. **85** (2009) 17006–p1.

[35] F. X. Wang, T. Wu, G. Wu, H. R. Liu, H. Chen, L. Y. Xie and H. X. Chen, New J. Phys. **11** (2009) 45003.

[36] Y. Mizuguchi and Y. Takano, J. Phys. Soc. Jpn. **79** (2010) 102001–1.

[37] C. de la Cruz, Q. Huang, J. W. Lynn, J. Li, W. R. I. an J. L. Zarestky, H. A. Mook, G. F. Chen, J. L. Luo, N. L. Wang and P. Dai, Nature, **453** (2008) 899.

[38] Q. Huang, Y. Qiu, W. Bao, M. A. Green, J. W. Lynn, Y. C. Gasparovic, T. Wu, G. Wu and X. H. Chen, Phys. Rev. Lett. **101** (2008) 257003.

[39] Y. Kawasaki, K. Deguchi, S. Demura, T. Watanabe, H. Okazaki, T. Ozaki, T. Yamaguchi, H. Takeya and Y. Takano, Solid State Comm. **152** (2012) 1135

[40] G. C. Cho, W. Kutt and H. Kurz, Phys. Rev. Lett. **165** (2012) 764.

[41] Y. Kawashima, K. Ichimura, J. Ishioka, T. Kurosawa, M. Oda, K. Yamaya and S. Tanda, Physica B: Condensed Matter **407** (2012) 1796.

[42] K. Ichimura, J. Ishioka, T. Kurosawa, K. Inagaki, M. Oda, S. Tanda, H. Takahashi, H. Okada, Y. Kamihara, M. Hirano and H. Hosono, J. Phys. Soc. Jpn. **77** (2008) Suppl. 151.

[43] Y. Kawashima, K. Ichimura, T. Kurosawa, M. Oda, S. Tanda, H. Takahashi, H. Okada, Y. Kamihara and H. Hosono, Physica C **470** (2010) S315.

[44] V. V. Kabanov, J. Demsar , B. Podobnik and D. Mihailovic, Phys. Rev. B **59** (1999) 1497.

[45] D. Dvorsek,V. V. Kabanov, J. Demsar , S. M. Kazakov, J. Karpinski and D. Mihailovic, Phys. Rev. B **66** (2002) 020510.

[46] H. J. Zeiger, J. Vidal, T. K. Cheng, E. P. Ippen, G. Dresselhaus and M.S. Dresselhaus, Phys. Rev. B, **45** (1992) 768.

[47] W. Albrecht, Th. Kruse and H. Kurz, Phys. Rev. Lett, **69** (1992) 1451.

[48] J. Demsar, K. Biljakovic and D. Mihailovic, Phys. Rev. Lett, **83** (1999) 800.

[49] T. Machida, K. Kogure, T. Kato, H. Nakamura, H. Takeya, T. Mochiku, S. Ooi, Y. Mizuguchi, Y. Takano, K. Hirata and Hideaki Sakata, J. Phys. Soc. Jpn, **81** (2012) 074714.

[50] M. Enayat, Z. Sun, U. R. Singh, R. Aluru, S. Schmaus, A. Yaresko, Y. Liu, C. Lin, V. Tsurkan, A. Loidl, J. Deisenhofer and P. Wahl, Sience, **345** (2014) 653.

[51] E. E. Rodriguez, C. Stock, P. Zajdel, K. L. Krycka, C. F. Majkrazak, P. Zavalij and M. A. Green, Phys. Rev. B, **84** (2011) 064403.

[52] T. Ishiguro, K. Yamaji and G. Saito, *Organic Superconductors*, *2nd Edition*, Springer, Berlin, 1997.

[53] M. Tinkham, *Introduction to Superconductivity*, *2nd Edition*, Dover, 2004